Diffusion Generated Motion for Recrystallization and Grain Growth

Matt Elsey, Selim Esedoḡlu, and Peter Smereka
Department of Mathematics, University of Michigan, Ann Arbor, MI 48109, USA

November 12, 2009

Abstract

A new numerical approach for the efficient computation of grain boundary motion is used to simulate normal grain growth and recrystallization in three dimensions with high accuracy. The method is based on the diffusion of signed distance functions and shares similarities with level set methods. The Herring angle condition at junctions and topological transitions are naturally captured with this formulation. In addition, this approach offers significant advantages over existing numerical methods and accurate computational results are presented on scales not previously possible. For example, a fully-resolved simulation of normal grain growth initially containing over 100,000 grains in three dimensions is presented. It is shown that the average grain radius grows as the square root of time and the grain size distribution is self-similar. This numerical approach is easily extended to include recrystallization. Simulations of recrystallization for physically relevant parameter values are displayed. These are quite difficult to obtain via kinetic Monte Carlo approaches, commonly used for this problem.

1 Introduction

Grain growth and primary recrystallization are two important ways in which the microstructure of polycrystalline materials (including most metals and ceramics) evolve during manufacturing processes. Statistical measures of the resultant microstructure affect important macroscale properties of the material, such as its conductivity and brittleness. Manufacturing processes must typically be tuned to provide for an optimal blend of desired material properties; however, performing such tuning experimentally is costly and time consuming. Therefore, simulations of these grain evolution phenomena have been attempted using a variety of numerical techniques.

Grain growth occurs when polycrystalline materials are annealed. The well-known model for grain growth [6, 20, 37] gives the grain boundary normal velocity as $v_n = \mu\gamma\kappa$, where μ denotes the boundary mobility, γ the surface tension, and κ the mean curvature of the boundary separating two grains. In some important cases (including the isothermal annealing of pure metals), it is a good approximation to take the mobility and surface tension to be constant. In this paper, we will restrict ourselves to the constant mobility and surface tension case, and set $\mu\gamma = 1$ for convenience. As shown in [40] and [63], this normal speed arises as gradient descent for the energy

$$E = \sum_{k<\ell} (\text{area of } \Gamma_{k\ell}), \tag{1}$$

where $\Gamma_{k\ell}$ is the interface between grains k and ℓ. The standard boundary condition for grain growth is the Herring angle condition [21], which for equal surface tensions states that triple junctions must meet at angles of 120°. This angle condition arises naturally from the algorithms used in the present paper, as shown in [14].

The phenomenon of recrystallization occurs when a polycrystalline material is simultaneously stressed and annealed. Grains with certain orientations are energetically favored by the stress, and grow at the expense of grains with other orientations. This process is modeled by the addition of a constant term to the normal velocity of grain boundaries separating the favored recrystallizing grains from unrecrystallizing grains. In the isotropic case, the normal velocity (outward from phase k) of interface $\Gamma_{k\ell}$ can then be written as

$$v_n(\Gamma_{k\ell}) = \kappa_{k\ell} + \lambda(e_\ell - e_k). \tag{2}$$

The parameter λ weighs the relative importance of the curvature motion and the constant normal speed at interfaces separating recrystallized ($e_k = 0$) and unrecrystallized ($e_k = 1$) grains. If phases k and ℓ are both recrystallized (or both unrecrystallized), $e_k = e_\ell$ and only curvature motion occurs along the interface $\Gamma_{k\ell}$. The additional constant term in the normal velocity is represented as a bulk energy term in the energy previously described by (1):

$$E = \sum_{k<\ell} (\text{area of } \Gamma_{k\ell}) + \lambda \sum_k e_k (\text{volume of phase } k). \tag{3}$$

In this work, we present a large-scale simulation of three-dimensional grain growth and a number of simulations of primary recrystallization in both two and three dimensions. The normal grain growth simulation in three dimensions starts from an initial condition containing over $130,000$ grains and simulates the evolution until only about $14,000$ remain. We present various statistics collected throughout this simulation. In particular, we demonstrate the anticipated self-similar character of the grain size distribution as it evolves in time. Furthermore, our results show good agreement with other three-dimensional predictions for grain growth, such as power law growth of the mean grain volume, and three-dimensional version of the Aboav–Weaire law and the Mullins extension of the two-dimensional von Neumann–Mullins relationship. These results compare well also with experimental and other simulation results where available.

The simulations of two-dimensional recrystallization allow for easy visualization of the effects of varying the value of the parameter λ in (3), which determines the relative importance of the curvature motion and the constant normal velocity motion. The theory of Johnson and Mehl, Avrami, and Kolmogorov (JMAK) [3–5, 25, 29] predicts sigmoidal growth of the recrystallized area fraction, and agrees well with our simulation results for large λ. For small λ, this theory is no longer applicable. We demonstrate the ability to simulate full recrystallization for values of λ comparable to those experimentally seen in real metals, a regime unattainable by Monte Carlo techniques [51], as further discussed in Section 4.6. We also present simulations with site-saturated and continuous nucleation in three dimensions, with good agreement with JMAK predictions given the choice of λ.

2 Algorithm and Previous Work

Our algorithm is an extension of *distance function-based diffusion generated motion* [14], which is in turn a variant of the *threshold dynamics* scheme proposed by Merriman, Bence, and Osher [36]. The threshold dynamics scheme reduces the computation of various geometric motions of an interface to the alternation of two highly efficient operations: convolution of a characteristic function representing the interior of the interface with a circularly symmetric kernel, and thresholding the convolution output to return to a characteristic function. On a uniform grid with N grid points, the complexity of these operations is just $O(N \log N)$ per time step. The method is also unconditionally stable, so that the only restrictions on the size of the time step are due to accuracy considerations. A major drawback of the threshold dynamics algorithm is that it is very inaccurate on uniform grids, because the interface must be represented as the boundary of a characteristic function, disallowing any possibility of sub-grid accuracy in the absence of adaptive grid refinement (as is explored in [46]).

A signed distance function-based algorithm for diffusion generated geometric motions of the same types attainable by threshold dynamics is proposed in [14]. This algorithm is a modification of the threshold dynamics algorithm, replacing the characteristic function of the set used in threshold dynamics with a signed distance function to the boundary of the set, and the thresholding operation by a redistancing operation. The redistancing operation reconstructs the signed distance function to the boundary of the set from the convolution output, much as the thresholding operation reconstructs the characteristic function of the set from convolution output in threshold dynamics.

Unlike the characteristic function of a set, the signed distance function is a Lipschitz continuous function. This allows for sub-grid accuracy in locating the interface on a uniform grid. Furthermore, fast algorithms are known for constructing signed distance functions (e.g. [44, 62]), so that the computational complexity of the signed-distance function based algorithm is still $O(N \log N)$ per time step. A more detailed discussion of the differences between [36] and [14] can be found in [14].

The threshold dynamics scheme was extended by Ruuth [45] to multiphase motion by mean curvature, the case occurring in grain growth, but the same accuracy limitations faced by the original threshold dynamics

scheme still apply. Standard level set techniques have also been applied to the grain growth problem in [15,63]. The level set method is a sharp interface method, similar to the signed distance function technique we use here (which may itself be considered a special type of level set method). Standard level set methods place only very loose restrictions on the details of the level sets used to implicitly represent the interface. For example, the size of the gradient $|\nabla\phi|$ of the level set function ϕ is generally restricted from becoming too large or too small. This restriction is insufficient for multiphase motion, as first noted and fully explained in [14]. In general, an $O(1)$ error is introduced in the motion of triple junctions due to differences in the profiles of the level sets representing the three phases. This error also prevents the correct angle conditions from being obtained.

In contrast, [14] provides analytical justification and extensive numerical convergence studies showing that the correct behavior is obtained at junctions under the multiphase version of the signed distance function-based algorithm for motion by mean curvature introduced there. The algorithm for multiphase motion is given in [14], with an enhancement allowing for the simulation of N grains using only $M \ll N$ signed distance functions described fully in [13]. This is achieved by representing large collections of individual, well-separated grains with a single signed distance function. Easily implemented precautions are taken to prevent non-physical interactions from occurring between grains contained in a single signed distance function.

The signed distance function-based algorithm for multiphase motion by mean curvature described there and applied in this work can be thought of as a particular type of level set method. In order to obtain the correct behavior at triple junctions, there is a stronger restriction on the level sets than ordinarily enforced; however, other hallmarks of the level set method are retained: the interfaces are implicitly represented (the algorithm operates only on the values of the signed distance function at grid points), the Lipschitz continuity of the level sets allows for sub-grid accuracy, and the interface is sharp (unlike phase field methods, in which the interface is represented by a diffuse transition layer). On the other hand, standard level set methods for evolution by mean curvature require the solution of a degenerate, highly nonlinear partial differential equation. In contrast, the present algorithm is unconditionally stable (allowing much larger time steps to be taken), a feature inherited from its close connection to the diffusion generated motion of threshold dynamics.

A number of other numerical methods have been used to simulate grain growth and primary recrystallization in previous work. One of the best-known techniques is the Monte Carlo Potts model [2, 50–52]. This model approximates curvature motion by a stochastic series of near-interface cell flipping steps. While the basic Monte Carlo method is quite easy to implement, it is extremely slow and lacks sub-grid accuracy. Furthermore, the stochastic nature of the Monte Carlo evolution ensures that some type of averaging is needed to approximate the true continuum motion. For example, the evolution of a simple circle by mean curvature is very difficult to capture accurately using Monte Carlo methods even on a well-resolved grid. Beyond these significant accuracy concerns, it is also difficult to connect the Monte Carlo method with some notion of "real" time beyond reorientation attempts. Also, as discussed in Section 4, attempts to simulate recrystallization for physically relevant values of the weighting parameter λ using Monte Carlo models were unsuccessful.

Front-tracking techniques have also been used to simulate mean curvature motion in both two [26,28] and three [28,54] dimensions. A major advantage of these techniques is computational efficiency, as computational resources are all devoted to the interface region. The fundamental difficultly inherent to this approach is managing the topological changes that abound in both grain growth and primary recrystallization. With explicit representations of the interface, it is difficult to check if curves (in two dimensions) or surfaces (in three dimensions) intersect. In the case of two-dimensional mean curvature multiphase motion, it is expected (though not fully proven, see [34]) that interfaces interact only through junction–junction collisions. If this conjecture is true, explicitly checking for and handling topological changes may be manageable in this case. However, *no such condition is expected to hold in three dimensions, or in the presence of bulk energy terms* such as those appearing in the energy for recrystallization (see equation (3)). Pinch-off can occur with only two phases in three-dimensional mean curvature motion (as in the standard "dumbbell" example), and is shown in this work also to occur in a two-dimensional recrystallization simulation in Section 4.5. Topological changes of this type are very difficult to detect, much less manage, using front tracking techniques, especially in three dimensions. In contrast, our algorithm handles topological changes naturally, without any user input or parameter choices.

The phase field technique has also been used extensively in simulations of grain growth [16, 19, 27, 30, 53] and is much more similar to our algorithm than Monte Carlo or front-tracking techniques. In the phase field

method, interfaces are implicitly represented. However, there must be a wide transition region representing the interface between grains. For example, Kim, et al. [27] report that at least six grid points are needed in the transition layer to achieve acceptable accuracy. Therefore, a grain needs to be on the order of at least 25 grid points across to be moderately resolved. In contrast, we demonstrate in [13] that we can simulate evolutions quite accurately with grains approximately ten grid points in each direction, and that we can track them down to half that length with only a few percent relative error. Though there is no rigorous notion of generalized solutions with uniqueness through topological changes, we also perform a convergence study in [13] showing that our simulations track grains through topological changes quite consistently as well. The large grain size requirement imposed by the phase field model is a serious impediment to performing very large-scale simulations.

Our algorithm has all the major advantages of these various computational approaches. It is closely related to both threshold dynamics and level set methods. From threshold dynamics, we inherit unconditional stability, allowing the choice of time step to be restricted only by accuracy considerations. From level set methods, we inherit sub-grid accuracy and graceful handling of topological changes, free from user input. As with front tracking models, we concentrate most of our computational resources at the interface, as the signed distance function computation (the most computationally intensive part of the algorithm) must be performed accurately only in a tubular neighborhood of the interface (with width proportional to $\sqrt{\Delta t}$). As a discretization of Mullins' PDE-based continuum description of grain boundary motion, our algorithm does not suffer from the difficulty of identifying physical time that plagues Monte Carlo-type models. However, the flexibility of the Monte Carlo method, which allows for the addition of a bulk energy term, application of various nucleation techniques, and relative weightings of surface tension-driven and bulk energy-driven motion in primary recrystallization, is also included in our algorithm. Indeed, the simple nucleation model we implement as part of our recrystallization simulations in Section 4 is taken directly from the Monte Carlo simulations of recrystallization performed by Srolovitz, et al., [50–52].

3 Normal Grain Growth

In this section, our algorithm for simulating normal grain growth will be described and a wide variety of statistical measures on the resulting grains will be presented.

3.1 Procedure

Our diffusion-based algorithm for multiphase motion by mean curvature is fully described in [13], but for the convenience of the reader we present a brief description. The initial condition was created by randomly placing $N(0)$ seeds in the computational domain and growing each simultaneously with constant normal velocity until another seed is encountered. Seed growth is stopped locally when seeds meet and globally when the domain is filled, resulting in a Voronoi-type initial condition. Given these $N(0)$ initial grains Σ_j^0, we partition them into $M \ll N(0)$ disjoint sets Ξ_k, such that $\cup_{j=1}^{N} \Sigma_j^0 = \cup_{k=1}^{M} \Xi_k$. We maintain M signed distance functions $d_k(x)$, giving the signed distance to the set Ξ_k, with $d_k(x) > 0$ for $x \in \Xi_k$. For example, in the first simulation described below we have $N(0) = 133,110$ and $M = 64$. The signed distance functions are updated using the following algorithm:

1. For $n = 0, \ldots, n_{\max}$, perform steps 2–5.

2. Form the convolutions $A_k(x) := K_{\Delta t} * d_k^n$ for $k = 1, \ldots, M$ where

$$K_{\Delta t} = G_{\Delta t} \text{ or } K_{\Delta t} = \frac{1}{4}\left(4G_{\frac{3}{2}\Delta t} - G_{3\Delta t}\right) \text{ with } G_{\Delta t} = \frac{1}{4\pi\Delta t} e^{-\frac{|x|^2}{4\Delta t}}.$$

3. Construct $B_k(x)$ for $k = 1, \ldots, M$ to remove overlaps and vacuums from the convolution:

$$B_k(x) = \frac{1}{2}\left(A_k(x) - \max_{\ell}\{A_\ell(x) : \ell \neq k\}\right)$$

4. Construct the signed distance function $d_k^{n+\frac{1}{2}}(x)$ for $k = 1, \ldots, M$ according to

$$d_k^{n+\frac{1}{2}} = \textbf{Redist}\left(B_k(x)\right).$$

5. If necessary, swap appropriate grains between signed distance functions to ensure that all the grains associated to given signed distance function remain well separated. Denote the resulting signed distance functions as d_k^{n+1}.

For a full description of the algorithm, the reader is referred to [13]. We use a simple cubic lattice with periodic boundary conditions to avoid introducing boundary effects into the evolution except in the case that a single grain grows so large as to be adjacent to itself across a periodic boundary. Such a case cannot arise in normal grain growth until only very few grains remain (e.g. $N(t) \ll 1,000$), which does not occur in the results reported here.

The computational complexity of our algorithm is formally $O(nk \log n)$, where k is the number of level set functions used, and n is the total number of grid points in each set. For a single signed distance function, both the convolution step and the redistancing operation are $O(n \log n)$. The algorithm is second-order accurate in space and first-order accurate in time away from triple points. At triple points, analysis and experiment in [14] suggest that the error is $O(\sqrt{\Delta t})$.

3.2 Normal Grain Growth Results

In this section, we present results of numerical simulation of normal grain growth in the unit cube with periodic boundary conditions. The cube has been discretized as a regular cubic lattice of size $512 \times 512 \times 512$. The coarsening rate is shown to agree well with theoretical predictions. The grain size distribution is calculated, and exhibits self-similarity. This distribution is compared with a number of different predictions from the literature. In addition, average numbers of grain edges, faces, and corners are computed and compared with other computational approaches and experimental data.

3.2.1 Qualitative microstructure

We present a three dimensional simulation with an initial condition containing 133,110 grains. The initial condition was generated as described in Section 3.1. Figure 1 shows a single grain taken from the simulation at 300 iterations; it appears to be very well resolved. Its faces, edges, and corners are easy to see. The faces are smooth, and most appear to be concave. Thus this particular grain, which is of average size at this stage in the evolution, must be growing due to the curvature of its interfaces. Overall, the grain resembles what is observed in real materials, such as the beta brass grain shown in Figure 2.

The coarsening of the grain pattern is demonstrated by Figure 3. Here we display the grains intersecting the $x = 0$, $y = 0$ and $z = 1$ surfaces in the initial condition (a) and after 300 iterations (b). Different colors correspond to different grains. By volume, the average grain at the end of the simulation is nearly ten times as large as the average grain at initial condition.

In Figure 4 we show all the grains from five of the sixty-four total set functions Ξ at 100 and 300 iterations. There is a great variability in the size of grains seen in this figure, from grains of only a single grid cell across which are about to disappear, to grains that are approximately fifty grid cells across in each direction.

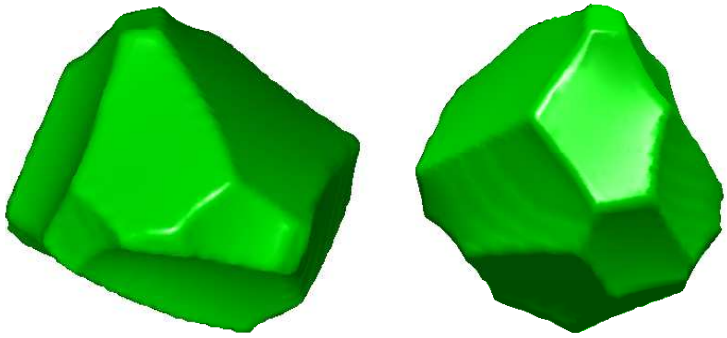

Figure 1: Two views of a single grain (corresponding to a 180° rotation in the xy-plane) chosen from the evolution after 300 iterations. This grain averages 21.2 pixels across in each dimension, equal to the average grain size at this point in the evolution. The grain is very well resolved, with faces, edges, and corners all easily distinguished.

Figure 2: A single grain of beta brass, approximately 2 cm in diameter, from the collection of W.W. Mullins. The photograph is due to K. Barmak and D. Kinderlehrer. The grain compares well to the simulated grain shown in Figure 1.

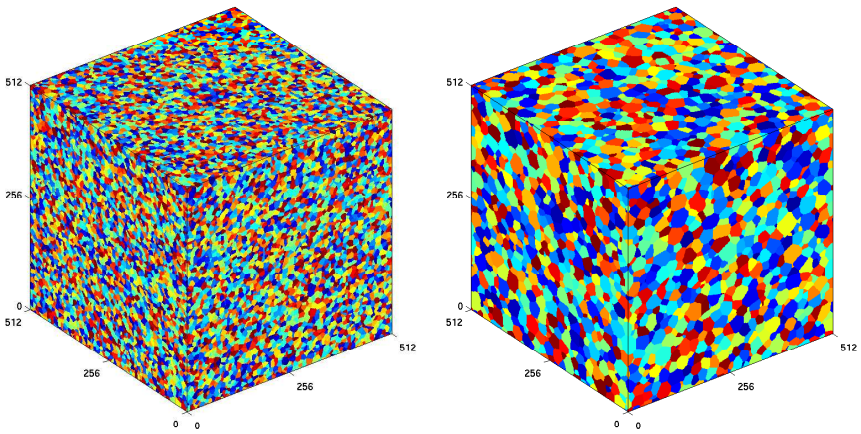

(a) (b)

Figure 3: Visualization of the grain pattern (a) at initial condition and (b) after 300 iterations. The initial condition contains 133,110 grains. After 300 iterations, 14,150 grains remain.

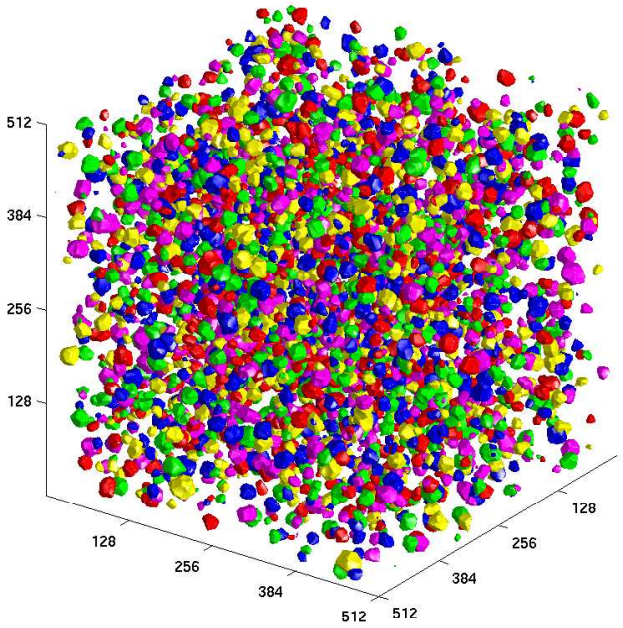

(a)

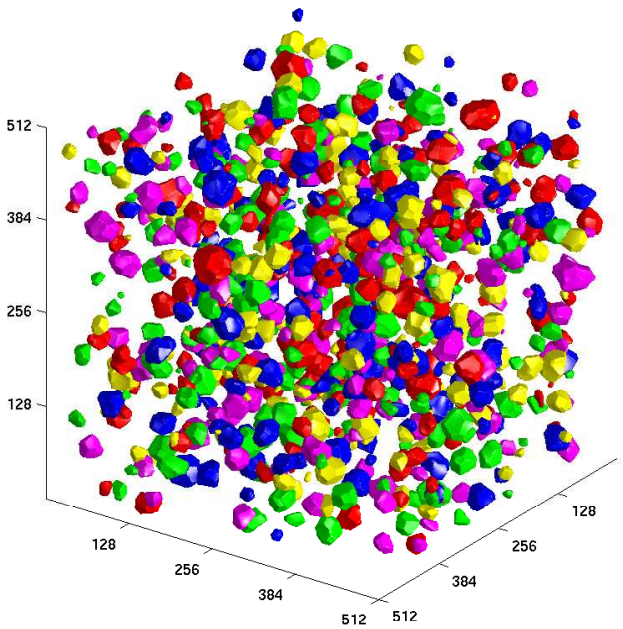

(b)

Figure 4: Grains from five of sixty-four level set functions in the simulation with initially 133,110 grains, after (a) 100 and (b) 300 iterations. At 100 iterations, there are 54,197 total grains. After 300 iterations, 14,150 grains remain. Only a subset of grains is shown, as otherwise the entire volume would be filled.

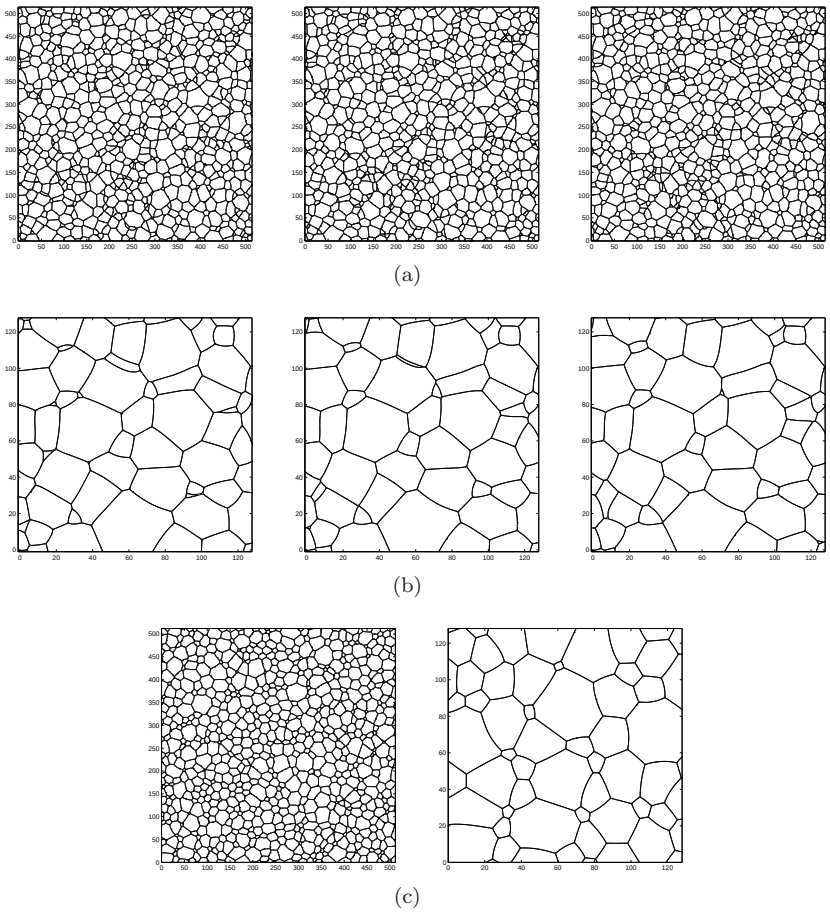

Figure 5: Three consecutive cross-sectional slices taken from simulation at 300 iterations. The full slice is shown in (a) and zoomed in on in (b). The curved nature of the interfaces is easily seen. The angles observed at triple junctions need not be 120° as the cross-section need not be oriented along the triple lines. (c) Two-dimensional simulation results. Triple junctions all meet at 120° angles and grain are more equiaxed, in contrast to the results seen in three-dimensional cross-section in (a) and (b).

Cross-sections of successive slices at 300 iterations are shown in Figure 5(a) and (b). Compare to Figure 5(c), showing results from a fully two-dimensional simulation, in which all three junctions must have 120° angles. The cross-sectional views also feature more grains that are long in one dimension and short in the other as compared to the two-dimensional simulation results, where grains tend to be more regularly shaped.

3.2.2 Energetics

It is known that, at least in the absence of topological changes, the surface energy E given by (1) decreases in time under mean curvature motion subject to the Herring angle condition at junctions. It is natural to expect that E would continue to decrease even through topological changes (critical events). We verified that our numerical scheme respects this fundamental behavior by evaluating the energy at every time step. We note that the energy E can be written in terms of the signed distance functions $d_k(x)$ and the Dirac delta function, $\delta(x)$, as the following sum of integrals over the computational domain Ω:

$$E = \frac{1}{2} \sum_{k=1}^{M} \int_{\Omega} \delta(d_k(x)) dx. \tag{4}$$

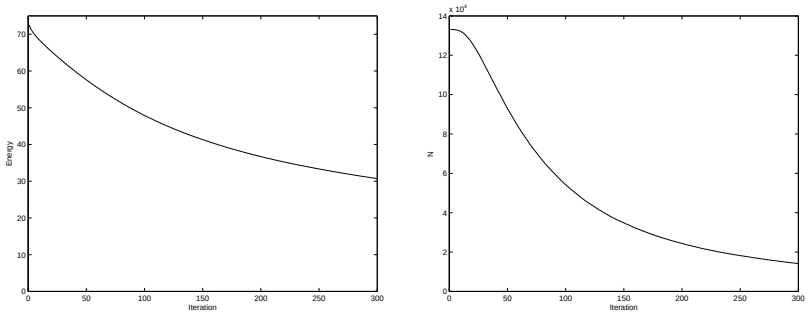

(a) (b)

Figure 6: (a) The energy $E = \sum_{i<j}(\text{area of } \Gamma_{ij})$ decreases monotonically at every iteration. (b) The number of grains N undergoes a short transition phase of slow decrease then decreases steadily from an initial value $N(0) = 133,110$ to a final value of $N(300) = 14,150$.

The factor of $\frac{1}{2}$ arises as this formula counts each interface twice. We discretize E as

$$E = \frac{\Delta x^2}{2} \sum_k \sum_{i,j,\ell} \tilde{\delta}(d_k(x_i, y_j, z_\ell)). \tag{5}$$

We utilize a first-order discretization of the delta function, $\tilde{\delta}$, following [47]. The energy E is measured at each time step and is found to decrease monotonically at every time step (see Figure 6(a)) even as the evolution naturally handles the topological changes involved in the disappearance of over 100,000 three-dimensional grains through 300 iterations. The evolution of the number of grains is shown in Figure 6(b). After a short transition period (approximately 20 iterations), the number of grains in the system decreases steadily. Notice that even during this transition period, the energy of the system is decreasing quickly. It should be pointed out that when formulating front tracking methods, one must "by hand" make sure that the energy decreases through topological changes whereas here it occurs naturally.

3.2.3 Grain growth rate and grain size distribution

The average grain size, $\langle R_V \rangle$, and the grain size distribution function, $f(R_V/\langle R_V \rangle)$, are probably the most important statistical quantities used to characterize a polycrystalline material. Here $R_V = (3V/4\pi)^{1/3}$ where V is the volume of a grain. Analytical approaches [18, 23, 32], experimental results (as reported in [2]), and simulation results, e.g. [2, 54], suggest that the average grain radius $\langle R_V \rangle$ exhibits power law growth as a function of time: $\langle R_V \rangle \approx Ct^n$, for t large. Analytically, the prediction $n = 1/2$ has been made using a variety of considerations. The experimental results reported in [2] find $1/4 \leq n \leq 1/2$. In their own simulation, [2] report that $n = 0.48 \pm 0.04$ for fits to long-time data (obtained by discarding data from the initial transition phase of the simulation). In [54], the authors show approximately linear long-time dependence of $\langle R_V \rangle^2$ on t. This simulation contains just 1000 grains initially, so the statistical precision of this measure is low. Furthermore, three-dimensional simulations via front tracking require that explicit assumptions be made on the types of topological changes that can occur.

As normal grain growth is characterized by the self-similarity of the distribution of $R_V/\langle R_V \rangle$, it follows that $\langle V \rangle \propto t^{3n}$. In Table 1, we fit $\langle V \rangle = \frac{1}{N(t)}$ to the function $at^b + c$, where $c \approx \langle V(0) \rangle$ and mollifies the effect of the initial grain size distribution on the fit. The fits are quite tight, with all reliability factors $< 0.7\%$. Equating $b = 3n$, we find that our simulation predicts $0.501 \leq n \leq 0.518$ with 95% confidence. The fit of $2.58t^{1.515} + 5.27 \times 10^{-6}$ to $\langle V \rangle$ is plotted in Figure 7.

The grain size distribution function $f(R_V/\langle R_V \rangle)$ is defined by

$$f(\xi)d\xi = \text{Proportion of grains with normalized radius } R_V/\langle R_V \rangle \in [\xi, \xi + d\xi). \tag{6}$$

In Figure 8, we show histograms for this distribution at a variety of stages in the simulation. The distribution changes greatly throughout the evolution. The initial condition is approximately the Voronoi condition for a

Time Interval	a	b	c	χ_1	χ_2	χ_3
$0 < t \leq 300\Delta t$	3.272	$1.550 \pm .004$	6.926×10^{-6}	3.79×10^{-3}	2.98×10^{-3}	2.29×10^{-3}
$50\Delta t < t \leq 300\Delta t$	2.743	$1.524 \pm .003$	6.471×10^{-6}	4.38×10^{-3}	2.28×10^{-3}	2.18×10^{-3}
$100\Delta t < t \leq 300\Delta t$	2.580	$1.515 \pm .005$	6.270×10^{-6}	4.86×10^{-3}	1.88×10^{-3}	1.57×10^{-3}
$150\Delta t < t \leq 300\Delta t$	2.603	$1.517 \pm .013$	6.303×10^{-6}	6.05×10^{-3}	3.22×10^{-3}	2.89×10^{-3}

Table 1: Fit of the data $\langle V(t) \rangle$, taken from the specified time interval, to $at^b + c$. b is given with 95% confidence interval. The reliability factor $\chi \equiv \sum_i |x_i^{obs} - x_i^{calc}| / \sum_i |x_i^{obs}|$, where *obs* denotes the observed value and *calc* denotes the calculated value from the fitted function. χ_1 gives the reliability factor computed over the interval $0 < t \leq 300\Delta t$, χ_2 over the interval $50\Delta t < t \leq 300\Delta t$, and χ_3 over the interval $100\Delta t < t \leq 300\Delta t$.

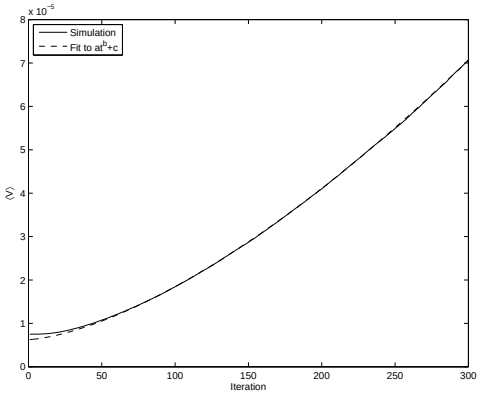

Figure 7: The average grain volume $\langle V \rangle$ compared to the best-fit power function $at^b + c$ fitted by non-linear least squares to the data from $100\Delta t < t \leq 300\Delta t$ (see Table 1). Aside from the brief transition period, the fit is indistinguishable from the simulation results.

randomly distributed set of points. The initial distribution of grain sizes is very narrow and sharply peaked. The distribution flattens out rapidly and appears to approach a self-similar state, characteristic of normal grain growth. This self-similar distribution appears to be attained by approximately 200 iterations and is maintained thereafter.

Another way to assess the self-similarity of the distribution of the grain size distribution function across iterations is to look at the evolution of the central moments of the various distributions obtained. For these distributions, the first moment is by definition 1 and the first central moment is always 0. The variance and skewness ($\mathbf{E}[(X - \mathbf{E}[X])^j]$, for $X = R_V/\langle R_V \rangle$ and $j = 2$ and 3, respectively) are plotted in Figure 9. These measures appear to be approximately constant for $t \geq 200\Delta t$, agreeing with the visual impression of self-similarity obtained from Figure 8(c).

Many closed-form distributions have been suggested as appropriate fits for the distribution $f(R/\langle R \rangle)$, including:

- The Louat distribution [32],
$$f_L(\xi) = 2\alpha\xi \exp(-\alpha\xi^2), \tag{7}$$
where α is a fitting parameter.

- The Hillert distribution [23],
$$f_H(u) = (2e)^\beta \frac{\beta u}{(2-u)^{2+\beta}} \exp\left(\frac{-2\beta}{2-u}\right), \tag{8}$$
where $u = R/R_{cr}$ and β is the dimensionality of the problem. In three dimensions, Hillert calculates $R_{cr} = \frac{9}{8}\langle R \rangle$, so $\xi \equiv R/\langle R \rangle = \frac{9}{8}u$, resulting in
$$f_H(\xi) = (2e)^3 \frac{64}{27} \frac{\xi}{(2 - \frac{8}{9}\xi)^5} \exp\left(\frac{-6}{2 - \frac{8}{9}\xi}\right). \tag{9}$$

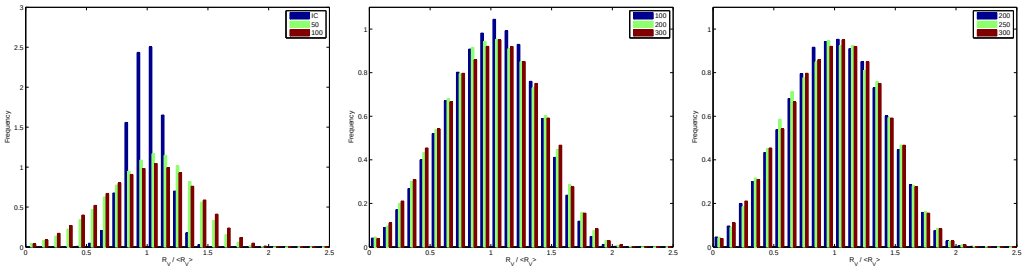

(a) (b) (c)

Figure 8: The distribution of $R_V/\langle R_V \rangle$ is shown at various times. (a) The distribution of the initial condition and after 50 and 100 iterations. The distribution is initially quite narrow but rapidly broadens. (b) At 100, 200, and 300 iterations. The distributions at 200 and 300 iterations are slightly wider than at 100 iterations and exhibit self-similarity. (c) At 200, 250, and 300 iterations, the grain size distributions appear to be self-similar.

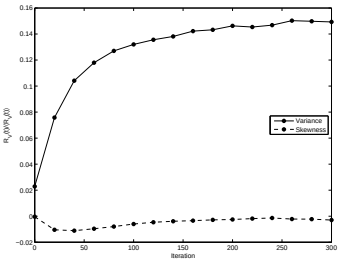

Figure 9: The variance and skewness of the distribution of $R_V(t)/\langle R_V(t) \rangle$ are compared across iterations. While the variance of the distribution in particular changes rapidly early in the evolution, the variance and the skewness of the distribution are approximately constant from 200 iterations and onwards, demonstrating the self-similarity of the distribution.

Grain size	log–normal			generalized Louat		Hillert	Rios		Weibull	
measure	μ	σ	χ	α	χ	χ	ν	χ	β	χ
R_A	0.074	0.574	0.335	0.685	0.152	0.389	2.14	0.221	2.07	0.171
R_V	0.056	0.417	0.282	0.741	0.330	0.128	3.34	0.031	2.80	0.104

Table 2: Least squares best-fit parameters and reliability factor χ for simulation data at 300 iterations (with 14,150 grains) to various distributions. The Rios distribution, with $\nu = 3.34$, fits the fully three-dimensional data very well. The observations made from two-dimensional cross-sections do not fit any of the distributions as well, but are best predicted by the generalized Louat distribution, with $\alpha = 0.685$. Note that the Weibull distribution does not fit the simulation distribution of $R_A/\langle R_A\rangle$ well, as the grain size distributions for two-dimensional growth and cross-sections of three-dimensional grain growth are known to disagree (for example, in [13]).

- The Rios distribution [42], a modification of the Hillert distribution (Hillert arises in the limit $\nu \to 4$):

$$f_R(\xi) = \frac{\xi\varepsilon^2 H_0 \nu^{H_0/2}}{(\varepsilon^2\xi^2 - \nu\varepsilon\xi + \nu)^{1+H_0/2}} \times \exp\left[-\frac{H_0\nu}{\sqrt{4\nu-\nu^2}}\left(\tan^{-1}\left(\frac{2\varepsilon\xi-\nu}{\sqrt{4\nu-\nu^2}}\right) + \tan^{-1}\left(\frac{\nu}{\sqrt{4\nu-\nu^2}}\right)\right)\right], \tag{10}$$

  where ε and H_0 are determined by the choice of the free parameter ν.

- The Weibull distribution, proposed by Fayad, Thompson and Frost [17] as a model for fully two-dimensional grain growth, occurring, for example, in thin-film experiments:

$$f_W(\xi) = \beta\left(\Gamma\left(1+\frac{1}{\beta}\right)\right)^{\beta}\xi^{\beta-1}\exp\left(-\left(\Gamma\left(1+\frac{1}{\beta}\right)\right)^{\beta}\xi^{\beta}\right), \tag{11}$$

  where β is a fitting parameter.

- The log–normal distribution is proposed in [18] as the distribution of grain radii in cross-sections of three-dimensional experiments.

$$f_{LN}(\xi) = \frac{1}{\sqrt{2\pi\sigma^2}\xi}\exp\left(\frac{-(\log\xi-\mu)^2}{2\sigma^2}\right), \tag{12}$$

  where $\log\xi$ is normally distributed with mean μ and variance σ^2.

These distributions are compared to the distribution of $\xi = R_V/\langle R_V\rangle$ in Figure 10(a). The Rios distribution (10), with $\nu = 3.34$, appears to fit our simulation data the best. The log–normal (12) and Louat distributions (7) fit quite poorly, showing the wrong behavior near $\xi = 0$, for large ξ, and also peaking at $\xi < 1$, all in disagreement with the simulation results. The Weibull (11) and Hillert distributions (9) show a better fit but can be seen both visually and by reliability factor (Table 2) to be inferior to the fit of the Rios distribution.

We also fit these distributions to data from cross-sections of the three-dimensional simulation. This is of interest as experimentally it is difficult to slice materials thinly enough for the experiments to be two-dimensional in nature; and it is also difficult to determine the volume of physical three-dimensional grains. It is easiest to take cross-sections of three-dimensional grains and measure areas and effective radii in cross-section. Defining $R_A = \sqrt{A/\pi}$, where A is the area of a grain in cross-section, we generate the distribution of $\xi = R_A/\langle R_A\rangle$ from the simulation data at 300 iterations. We take 512 cross-sections of constant z-value and aggregate the grain slice area data across all these cross-sections to create the simulation distribution. These cross-sections contain a total of 368,138 two-dimensional grain slices. In Figure 10(b), we fit this distribution to the closed-form distributions discussed previously. None of these distributions fit the cross-sectional data as well as the Rios distribution fit the fully three-dimensional data taken from grain volumes. The Louat distribution fits the data the best with $\alpha = 0.685$ but with a reliability factor of $\chi = 0.152$. For comparison, the Rios distribution fits the three-dimensional data with $\chi = 0.031$. Figure 10(c) compares the simulation distributions of $\xi = R/\langle R\rangle$ for $R = R_V$ and $R = R_A$ (from the three-dimensional data, and from cross-sections of the three-dimensional simulation, respectively). The distribution of $R_A/\langle R_A\rangle$ is much flatter and

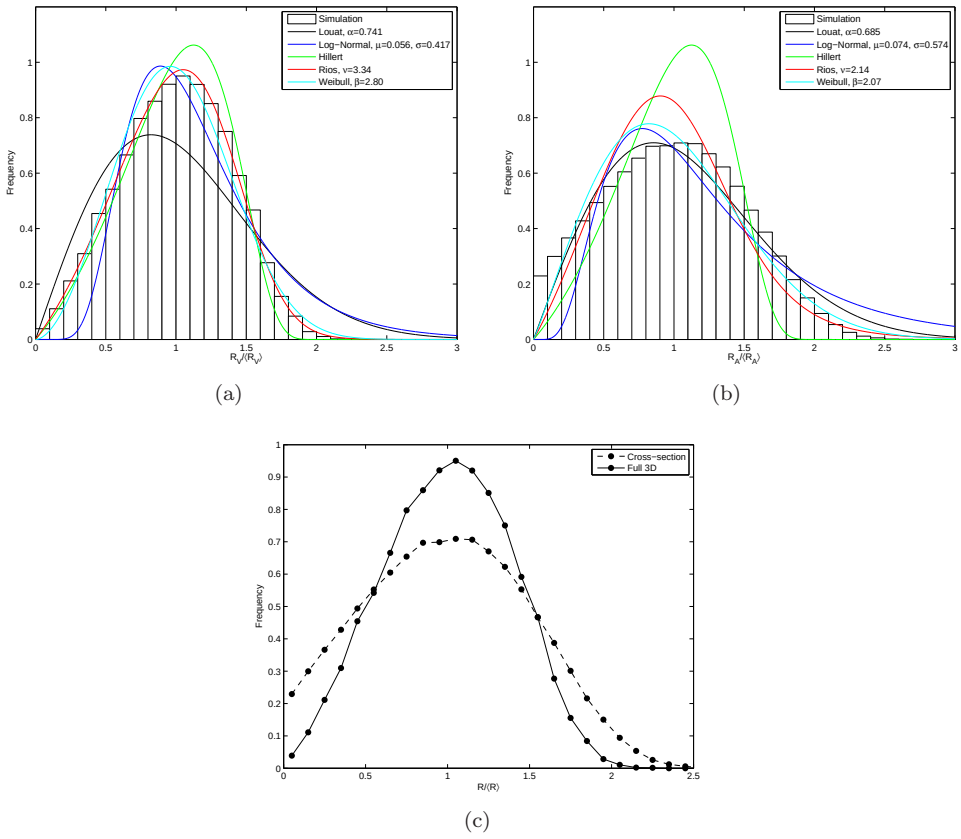

(a) (b) (c)

Figure 10: (a) Comparison of the distribution of $\xi = R_V/\langle R_V\rangle$ at 300 iterations (with 14,150 grains) to least squares best-fit predictions to Louat, log–normal, Hillert, Rios and Weibull distributions. Note that the Louat, log–normal and Weibull distributions predict the peak of the distribution to occur at $R_V/\langle R_V\rangle < 1$, while the simulation distribution peaks to the right of 1. The peak of Hillert's distribution occurs at $R_V/\langle R_V\rangle = 9/8$, agreeing well with our simulation results. However, the Hillert's distribution predicts a higher peak and narrower distribution than we find in the normal grain growth phase. The Rios distribution is a modification of the Hillert distribution and matches the simulation results well. (b) Comparison of the distribution of $\xi = R_A/\langle R_A\rangle$ at 300 iterations (with 368,138 grains taken from the 512 cross-sections of constant z-value) to least squares best-fit predictions under the same distributions. In cross-section, the data best fits the generalized Louat distribution, though the fit is not tight. (c) Comparison of the distribution functions for radius computed from volume ($R_V = (3V/(4\pi))^{1/3}$) from three-dimensional simulation data and for radius computed from area ($R_A = \sqrt{A/\pi}$) from cross-sectional data taken from three-dimensional simulation. The distribution is much flatter and wider for cross-sectional data.

wider than the distribution of $R_V/\langle R_V\rangle$, reemphasizing the importance of interpreting these distributions separately.

3.2.4 Topology

Interesting topological characteristics of the grain network include the number of faces, corners and edges of individual grains in three dimensions, and the number of edges of grains viewed in cross-section. Such characteristics have been the subject of numerous experimental studies (e.g. [10, 24, 41, 60, 61]). Here we compare the topological measures extracted from our large 3D simulation to those obtained from experimental data as well as to those from other simulations. In all the following results, we take data from $T = t_{\text{final}} = 300\Delta t$. At this time, 14,150 grains remain. In the 512 cross-sections of constant z-value, there are a total of 368,138 grain slices.

In order to count faces, corners and edges of individual grains at any fixed time T in the evolution, each grid point in the discretization is assigned a value from the set $\{1, \ldots, N(T)\}$ corresponding to the grain at that location. The number of faces of grain i is then the number of unique identifiers different from i contained in a 1-neighborhood of the set of grid points that have identifier i. Counting corners is more

	$2\langle e\rangle/\langle f\rangle$	$\langle f\rangle$	$\langle c\rangle$	Reference
Simulation	5.12	13.79	23.52	
Potts model Monte Carlo simulation	5.14	12.85	22.19	[2]
Potts model Monte Carlo simulation	—	13.7	—	[57]
Vertex dynamics	5.01	13.8	—	[58]
Phase field simulation	5.07	13.7	23.1	[30]
Surface Evolver simulation	5.05	13.5	22.6	[55]
Pentagonal dodecahedron	5	12	20	[49]
Tetrakaidecahedron	5.143	14	24	[48, 59]
Voronoi model	5.27	15.54	27.07	[35]
Johnson–Mehl model	5.10	13.27	22.56	[35]
Austenite grains	—	12.6–13.4	—	[31]
1015 α–iron grains	—	12.1	—	[61]
30 β-brass grains	5.142	14.5	24.852	[10]
β-brass grains	4.92	11.16	—	[24]
100 Al–Sn alloy grains	5.06	12.48	21.04	[60]

Table 3: Summary of topological data for simulations, regular polyhedra, and experiments. $2\langle e\rangle/\langle f\rangle$ gives the mean number of edges per face, while $\langle f\rangle$ and $\langle c\rangle$ give the mean number of faces and corners, respectively. In [31], the authors report that $\langle f\rangle$ increases as a function of annealing time, through 50 minutes.

challenging. In three dimensions, corners are characterized as being locations where four or more grains come together. We denote the set of all such locations as C. Because adjacent grid locations may, as part of a highly resolved corner, be marked as each being such a location, we take the number of connected components of C (as opposed to simply the number of points in C) within a single grain to be the number of corners possessed by that grain. However, this procedure will cause two corners connected by a short edge to be counted as one. To alleviate this problem, we subdivide the grid twice before applying the above procedure (so that a grid of size $n \times n \times n$ is subdivided to size $4n \times 4n \times 4n$ before counting vertices). Having thus counted the number f of faces and the number c of corners as described above, we appeal to the well-known formula $c - e + f = 2$ of Euler to infer the number e of edges of each grain. This formula holds for all polyhedra that are topologically equivalent to the sphere, which appears by inspection to be true for all the grains in our simulations of grain growth.

Data for the mean number of edges per face, mean number of faces, and mean number of corners is presented in Table 3 and compared to other simulations, to data reported for some regular polyhedrally-based grain models, and experimental results. The summary statistics vary some with the simulation technique. Ours are well within the range of values found with other simulation techniques (though the other simulations were smaller and must be less statistically valid whether due to a smaller number of grains or the potential effects of ensemble averaging). Regular polyhedra such as the pentagonal dodecahedron and the tetrakaidecahedron have been proposed as space-filling approximations for grain shapes [35, 48, 59], though experimentally it is well-known that grains come in a variety of shapes and sizes. The tetrakaidecahdron matches the mean values we found well, but cannot explain more complex features of grain growth, such as the grain size distribution function (6). The Voronoi model is generated by distributing seeds uniformly at random and growing crystals simultaneously and isotropically from these seeds. The Johnson–Mehl model grows crystals isotropically but allows for varying nucleation times [35]. Both these models ignore grain boundary motion due to interface curvature, holding grain boundaries stationary once crystals meet. These are in fact models for recrystallization, which we discuss in Section 4, with an energy given by (3), in the limit $\lambda \to \infty$. The experimental data contains a wide range of values, clearly demonstrating the difficulty of computing these measures in three dimensions and also suggesting that other higher-order effects (such as variable surface tension and mobility due to grain boundary misorientation and inclination) play an important role in the evolution of polycrystalline grain systems. In future work, we will investigate extending our algorithm so that such effects can be simulated.

In Figure 11, we plot the frequency with which grains with f faces occur. The distribution is skewed towards grains with many faces. The peak occurs at $f = 12$ faces and the mean number of faces is $\langle f\rangle = 13.79$. It is natural to expect that larger grains will have more faces, on average. However, the exact nature of this

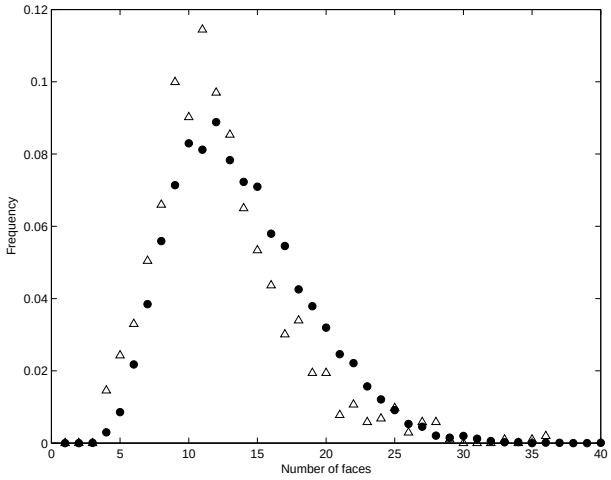

Figure 11: The proportion of grains with a given number of faces is plotted (solid circles). The peak occurs at $f = 12$ faces. Experimental data from [61] is also plotted (triangles). Note that this experimental data predicts a smaller mean number of faces (12.1) than other experimental and simulation data. See Table 3.

relationship is unknown. Figure 12 shows the relationship between the mean value of $R_V/\langle R_V\rangle$ for grains with f faces and f, as determined from our simulation data. We also compare with measurements made by Rhines and Patterson [41] on aluminum, by Zhang, et al. [61], on α-iron, and with simulation data generated by Anderson, et al. [2], using a Potts model and kinetic Monte Carlo techniques. The fit, particularly to the data for aluminum, is quite good and appears to describe the experimental data better than the linear fit posited in [2]. The simulation results of Anderson, et al., do appear to fit the measurements of Zhang, et al., well for small f, but poorly for large f.

In Figure 13(a), the mean number of corners for grains with f faces is plotted against f. Stable corners occur where three triple lines come together. Under the assumption that every corner is stable, $3c = 2e$. Together with Euler's formula, we can then calculate the number of corners and edges as a function of the number of faces f as $c(f) = 2(f-2)$ and $e(f) = 3(f-2)$. This prediction of a linear relationship between c and f is also plotted in Figure 13(a), and agrees very well with the values obtained by counting corners using the method described above. Note that Figure 11 illustrates that very few grains have less than 4 or more than 30 faces, so small inaccuracies in the count or the presence of only a few unstable corners will cause the small deviations from the prediction shown. Figure 13(b) shows similar correspondence between the simulation-determined values and the predicted values for the mean number of edges per face among grains with f faces.

The three-dimensional version of the Aboav–Weaire law [1, 56], proposed by Edwards and Pithia in [12] provides a relationship between the number of faces f exhibited by a grain and the mean number of faces of its neighboring grains, M_f:

$$M_f = \langle f\rangle - 1 + \frac{\langle f\rangle + \mu_f}{f}, \tag{13}$$

where μ_f is the variance of f. Following Wakai, et al., [54], we plot the mean value of $\langle fM_f\rangle$ against f and find the linear relationship predicted by Edwards and Pithia, but find the best linear fit to be $fM_f = 13.6f + 25.4$. This is in good agreement with the results of Wakai, et al., who found $fM_f = 13.3f + 23.4$. Based on their experimental data, Zhang, et al. [61] found $fM_f = 13.97f + 12.61$. Equation (13) predicts $fM_f = 12.8f + 37.7$, using the values of $\langle f\rangle$ and μ_f determined by our simulation data. Thus simulation, experiment, and theory for the three-dimensional Aboav–Weaire law agree well up to an additive constant. See Figure 14(a) for simulation data and best fit line.

In two dimensions, the well-known von Neumann–Mullins relationship [37] states that grains with more than six sides grow, and grains with fewer than six sides shrink:

$$\frac{dA}{dt} = \frac{\pi}{3}(n-6), \tag{14}$$

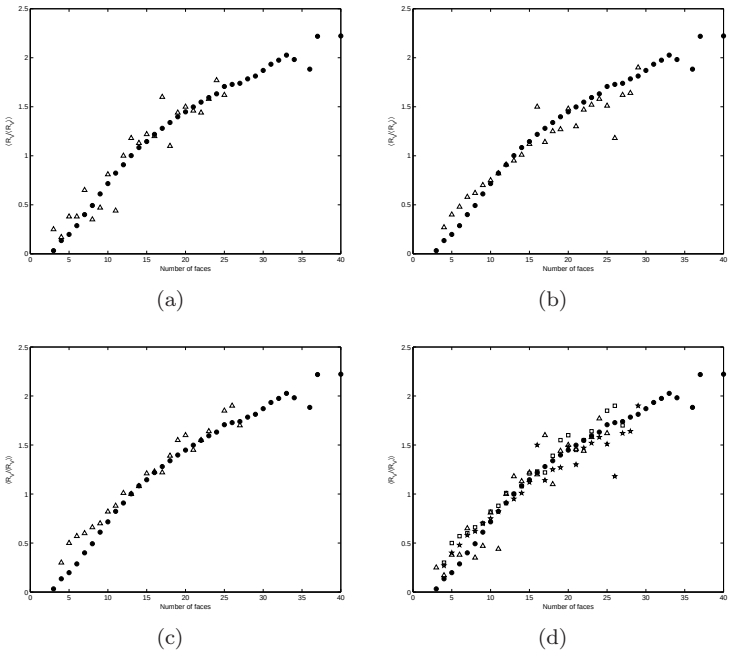

Figure 12: The relationship between the number of faces f and the mean value of $R_V/\langle R_V \rangle$ for grains with f faces is plotted (solid circles) and compared to (a) measurements for Al [41], reproduced from [2], (b) measurements reconstructed from serial sections of α-iron [61], (c) simulation data of Anderson, et al. [2]. In (d), all three are shown for comparison, with Al data marked by triangles, α-iron data by stars, and Anderson, et al. simulation data by squares.

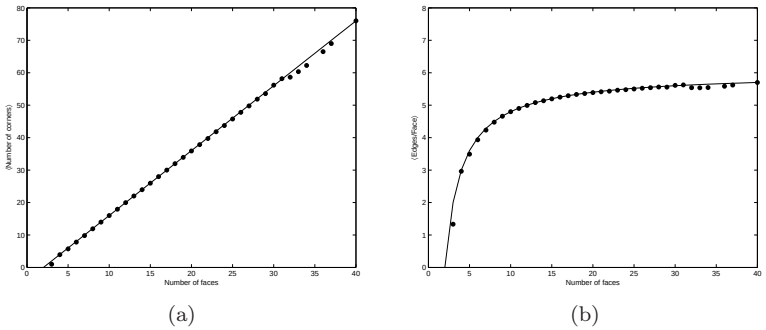

Figure 13: (a) There appears to be a linear relationship between the number of faces f and the mean number of corners among grains with f faces. (b) The mean number of edges per face for grains with f faces is plotted against f. The solid line is the mean number that would occur if each corner is the meeting of exactly three edges. The good correspondence between the simulation results and this prediction indicates that the number of corners is being counted accurately.

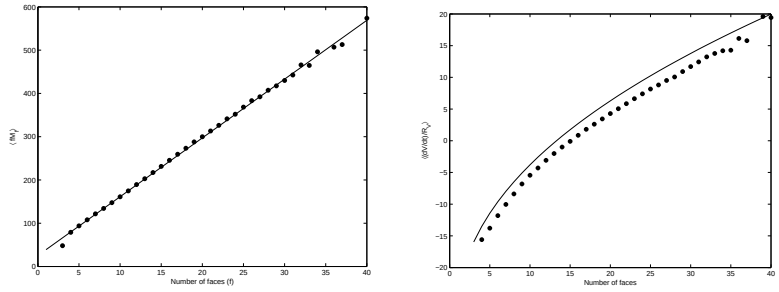

(a) (b)

Figure 14: (a) $\langle fM_f \rangle$, the mean of the product of the number of faces of a grain and the mean number of faces of its neighbors grows linearly as a function of f, matching well with the simulation results of Wakai, et al. [54]. (b) Comparison of the number of faces, f, to the mean growth rate $\langle (dV/dt)/R_V \rangle$ for grains with f faces. Simulation data from $290\Delta t \leq t \leq 300\Delta t$ is plotted. The three-dimensional von Neumann-Mullins prediction is plotted as a solid line for comparison.

where n is the number of sides of the grain. Mullins [38] proposed the following relationship for three dimensions, relating the growth rate of a three-dimensional grains to the number f of its faces:

$$\left\langle \frac{1}{R_V} \frac{dV}{dt} \right\rangle = F(f)G(f), \tag{15}$$

where

$$F(f) = \frac{\pi}{3} - 2\tan^{-1}\left(\frac{1.86\sqrt{f-1}}{f-2}\right) \tag{16}$$

and

$$G(f) = 5.35 f^{2/3}\left(\frac{f-2}{2\sqrt{f-1}} - \frac{3}{8}F(f)\right)^{-1/3}. \tag{17}$$

In Figure 14(b), we plot the simulation results for $\langle (dV/dt)/R_V \rangle$, taken from $290\Delta t \leq t \leq 300\Delta t$. Due to the large scale of our simulation, we were only able to store output data from every other iteration. For grains persisting throughout the given time range, we used centered differencing in time to approximate $dV/dt = (V(t+2\Delta t) - V(t-2\Delta t))/(4\Delta t)$ for $t = 292\Delta t, 294\Delta t, 296\Delta t, 298\Delta t$. The simulation results follow the same curve as the predictions but appear to differ by a constant additive value of approximately 2.2. Our simulation results agree well with those of Wakai, et al. [54] (using Surface Evolver, a front-tracking software package), and Weygand and Bréchet [58] (via vertex dynamics). Recently, MacPherson and Srolovitz [33] published a generalization of the von Neumann–Mullins relationship to three dimensions; however the quantities involved in their formula are quite difficult to calculate numerically. We elect to compare only to the Mullins generalization, which depends only on the number of faces f.

4 Recrystallization

Recrystallization is an important process for microstructural development in polycrystals. In this process, grains with lower bulk energy nucleate within existing grains having higher bulk energies. The nucleated grains can then grow due to the difference in their bulk energies. This process has been studied for over seventy years. Burke and Turnbull [8] gave a classic review of recrystallization in 1952. For a more recent review, see Doherty, et al. [11].

4.1 Model

The model for recrystallization we shall use is the one used by Srolovitz, et al. in [50–52]. The growth of a recrystallized grain is obtained by the addition of a constant term to the normal velocity of grain boundaries

separating the favored recrystallizing grains from unrecrystallizing grains. In the isotropic case, the normal velocity (outward from phase k) of interface $\Gamma_{k\ell}$ can then be written as

$$v_n(\Gamma_{k\ell}) = \kappa_{k\ell} + \lambda(e_\ell - e_k). \tag{18}$$

The parameter λ weighs the relative importance of the curvature motion and the constant normal speed at interfaces separating recrystallized ($e_k = 0$) and unrecrystallized ($e_k = 1$) grains. If phases k and ℓ are both recrystallized (or both unrecrystallized), $e_k = e_\ell$ and normal grain growth ensues. An important feature of recrystallization is nucleation. We shall follow the models proposed in [51] in which each spatial location is equally likely to be chosen as a nucleation site for a circular (spherical, in three dimensions) grain with a size probabilistically determined (but chosen to be small relative to the mean grain size). Nevertheless, we will see that heterogeneities in the recrystallization pattern can arise as a consequence of the dynamics in certain regimes of the parameter λ (in agreement with [52]). Further we shall consider two possible models for the nucleation, namely *site-saturated* and *continuous*. For site-saturated recrystallization a fixed number of grains are nucleated at a particular time and random locations. For continuous recrystallization grains are nucleated at a constant rate at randomly chosen locations.

4.2 JMAK Theory

A normal velocity of the form (18), in the limit $\lambda \to \infty$, is in keeping with the well-known recrystallization theory independently developed by Johnson and Mehl [25], Avrami [3–5], and Kolmogorov [29] (JMAK). JMAK theory is based on the assumption that each nucleated grain grows outward with constant normal velocity, which occurs in our system by neglecting the curvature term, and is approximated by choices of λ sufficiently large that the bulk energy term dominates the interfacial energy term in (3). The JMAK model has associated theoretical results in this limit, predicting the recrystallized volume fraction F to be a sigmoidal function of time, t, in the form

$$F(t) = 1 - \exp(-kt^p), \tag{19}$$

where k and p are constant. The parameter p can be predicted given the nucleation technique and the dimensionality of the evolution [9].

4.3 Previous Work

Recrystallization has been simulated mainly with Monte-Carlo Potts models [50–52] and cellular automata models [22]. As pointed out in [43], these techniques have drawbacks. In the Monte Carlo models already mentioned, the ratio H/J of two of the parameters in the notation of [43] — where H is the weight of the bulk energy term and J is that of the surface energy term up to a resolution dependent factor — plays the role of λ in (3). One difficultly with Monte Carlo simulations is that the stochastic nature of the model introduces roughness into the boundaries for large H/J, rather than providing the constant normal velocity expected for recrystallization. Furthermore, the boundary migration rate does not depend in a linear way on the ratio H/J along surfaces with zero curvature, while the migration rate for our model, given by (18), clearly varies linearly with λ along such surfaces.

The cellular automata model does give the constant normal velocity expected to result from the bulk energy term, but the technique does not incorporate the interfacial (surface) energy term into the model, and simulation results are highly dependent on the details of the local interactions. A hybrid model combining the Monte Carlo Potts model and cellular automata was investigated in [43]. One difficultly with this model is in linking the Monte Carlo model to the cellular automata appropriately to capture the relative importance of interfacial and bulk energies of the system.

The correspondence between the ratio of parameters H/J in the Monte Carlo model of Srolovitz et al. [50–52], and our parameter λ is $\lambda \approx (n/2) \times (H/J)$, where n is the number of grid points along one dimension. In [51], the authors report that metallic systems undergoing recrystallization have H/J in the range 0.01–0.1, corresponding to λ in the range $n/200$–$n/20$. The simulations in [51, 52] take H/J in the range 0.5–2 resulting in heterogeneous nucleation and H/J in the range 3–5 yielding homogeneous nucleation. Only in the case of very large recrystallized grains, more appropriate of abnormal grain growth (also known as

secondary recrystallization) than primary recrystallization (see [50]), can the authors simulate the evolution using $H/J = 0.1$. We perform simulations of primary recrystallization with $n = 4096$ and λ as small as $4096/40$, corresponding to $H/J = 0.05$.

Recrystallization has also been modeled recently via a vertex model [39] and in a level set framework [7]. It is difficult to simulate nucleation (which necessarily produces new vertices that must be connected to existing vertices) and to accurately calculate curvature using the vertex model. The level set method in [7] does not include motion by mean curvature, but only motion due to the constant normal velocity arising from bulk energy differences across interfaces. Multiphase, constant normal velocity motion suffers from non-uniqueness in the absence of curvature effects, even when away from topological changes. Vanishing curvature limit is one way to select a solution [40], but the motion computed in [7] is not this solution. Moreover, in practice, curvature effects (grain growth) are not negligible during recrystallization.

4.4 Procedure

The extension of our algorithm from Section 3.1 to the context of recrystallization, i.e. to interfacial velocities of the form (18), consists of replacing Step 2 of that algorithm by:

$$\boxed{A_k(x) := K_{\Delta t} * d_k^n - 2\lambda \Delta t e_k}$$

We recall that we set $e_k = 1$ for sets containing unrecrystallized grains, and $e_k = 0$ for sets containing recrystallized grains. We demonstrate this extension with simulations of primary recrystallization in both two and three dimensions. Two dimensional simulations are useful for visualization of the microstructure. In three dimensions it is difficult to visualize whole grains. However, most experimental systems of interest are fully three-dimensional, so statistical measures are of much greater value when obtained from three-dimensional simulations instead of two-dimensional simulations. In two dimensions we demonstrate the effect of varying λ, the parameter weighting the relative contributions of the interfacial and bulk components of the energy. In three dimensions we explore site-saturated and continuous nucleation, and the effect of these different nucleation processes on the grain size distribution function.

4.5 Two-dimensional site-saturated recrystallization

We first simulate recrystallization in two dimensions, where microstructure is easier to visualize. This allows for a qualitative understanding of the effect of the parameter λ in recrystallization simulations. We discretize the unit square into a uniform 4096×4096 grid ($\Delta x = 1/4096$). Each simulation takes the same initial condition, with 4,209 circular grains nucleated at sites chosen uniformly at random onto a grain pattern initially containing 30,842 unrecrystallized grains. The radius of nucleated grains was normally distributed with mean $4.9\Delta x$ and standard deviation $2\Delta x$. The normal distribution was modified so that any grain assigned a radius less than Δx was reassigned radius Δx, preventing the occurrence of extremely small grains or complications from attempting to assign a negative radius to a nucleating grain.

From (18), it follows that a circular nucleated grain completely contained within an unrecrystallized grain (i.e. not straddling any grain boundaries) should remain stationary if its radius is equal to $1/\lambda$, as $\kappa = -1/r$ for a circular grain. In the first test, we choose $\lambda = 4096$, so that the critical grain radius is Δx. All nucleated grains are expected to grow (though some may be nearly stationary), and we expect that this simulation is a good approximation of homogenous nucleation as described by the JMAK formalism. Indeed, after a short transition period (approximately 10 iterations, through which 6.8% of the area is recrystallized), a log-plot of time against $-\log(1-F)$, where F is the recrystallized area fraction, appears to be nearly linear, suggesting a relationship between time and F of the form of (19).

The second simulation takes $\lambda = 4096/10$, making the critical grain radius $10\Delta x$, 2.5 standard deviations larger than the mean nucleated grain radius. We expect that only a small subset of the nucleated grains will survive and grow — those that are initially very large and those that are sufficiently large and in energetically favorable positions. In particular, nucleated grains crossing grain boundaries and especially triple junctions are more likely to survive than those contained entirely within an existing grain. Consequently, one is in a regime in which heterogeneous nucleation results. This is similar to the simulation performed using Monte Carlo techniques by Srolovitz, et al. [52].

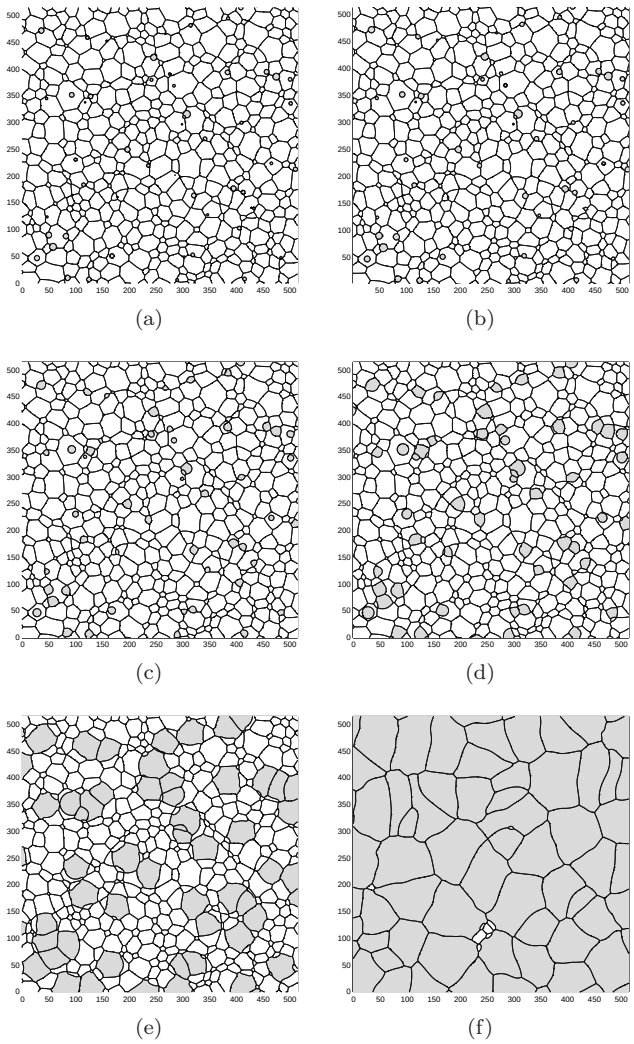

Figure 15: A 512×512 section of the two-dimensional recrystallizing grain pattern with $\lambda = 4096$ after (a) 1, (b) 2, (c) 5, (d) 10, (e) 25, and (f) 75 iterations. Recrystallized grains are shaded in gray. At these times, 0.8%, 1.2%, 2.6%, 6.8%, 30.5%, and 96.0% of the area is recrystallized, respectively. Nearly all nucleated grains grow, almost irrespective of their surroundings.

In contrast to the first simulation, with $\lambda = 4096/10$, recrystallization proceeds much more slowly (Figure 17(a) and (b)). Also, only 495 of the original 4,209 nucleated grains remain after recrystallization. In this simulation, the recrystallized area fraction decreases initially, reaches a minimum near 25 iterations, and then increases throughout the rest of the evolution. The JMAK formalism, predicting sigmoidal growth, is insufficient to model the early stages of the evolution of the recrystallized area fraction in this situation (see Figure 17(c)), as (19) is strictly increasing for $t > 0$. Later in the evolution, the JMAK prediction is well-satisfied by this evolution, as demonstrated by the near-linearity of this plot at later times.

4.6 Two-dimensional continuous recrystallization

To show the potential for our algorithm to simulate recrystallization with bulk energy differences similar to those seen in recrystallization of metals, we perform a simulation with $\lambda = n/40$, corresponding to $H/J \approx 0.05$. Here, the critical radius is $40\Delta x$, far larger than any nucleated grain. Thus, for nucleated grains to grow, they must be situated across grain boundaries or triple junctions, and may also need to group together spatially with other recrystallized nuclei. In this regime, the majority of nucleated grains will disappear quickly. To achieve recrystallization, we perform continuous nucleation, still with grain radii

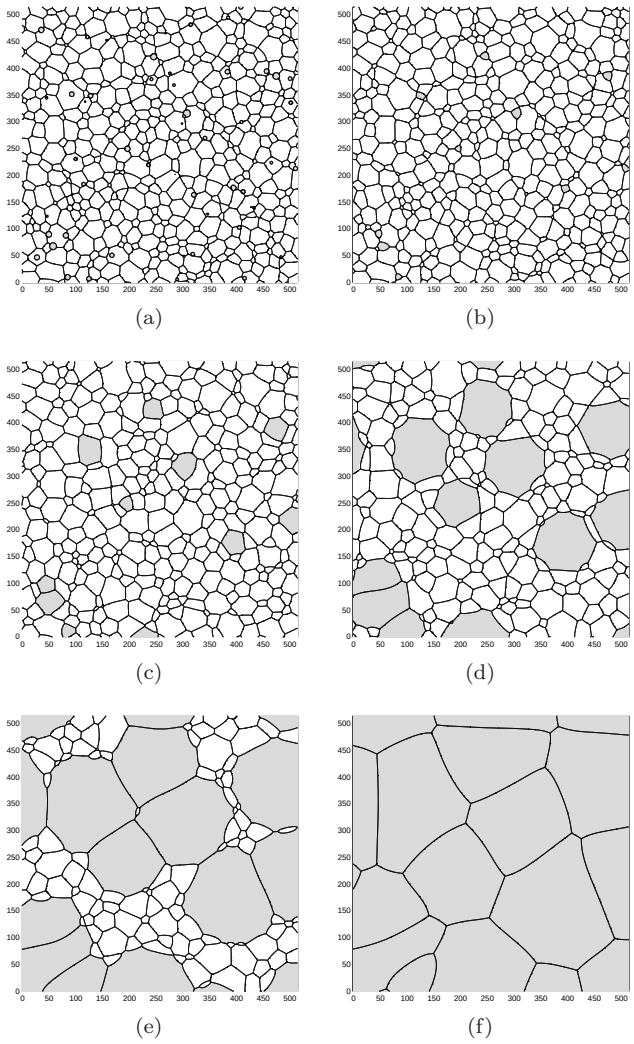

Figure 16: A 512×512 section of the two-dimensional recrystallizing grain pattern with $\lambda = 4096/10$ after (a) 1, (b) 75, (c) 275, (d) 610, (e) 905, and (f) 1760 iterations, corresponding to 0.8%, 0.7%, 4.9%, 25.1%, 50.1%, and 95.0% recrystallized area, respectively. The time of evolution for (b) corresponds to the time of evolution for Figure 15(f), emphasizing the effect of varying λ. Recrystallized grains are shaded in gray.

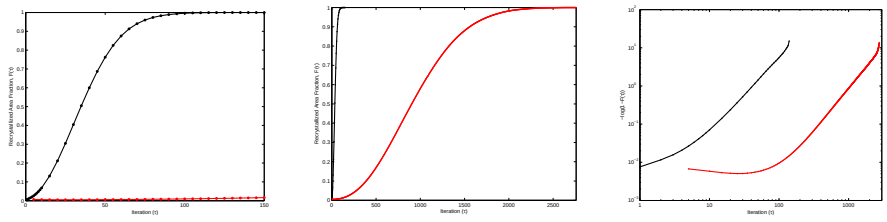

Figure 17: Comparison of results for two-dimensional site-saturated nucleation recrystallization simulations with $\lambda = 4096$ (blue) and $\lambda = 4096/10$ (red) on the same microstructure of unrecrystallized grains. (a) and (b) The recrystallized area fraction grows much more quickly for $\lambda = 4096$ than for $\lambda = 4096/10$. (c) The simulation with $\lambda = 4096$ satisfies the JMAK prediction well after approximately $\tau = 25$ iterations. The simulation with $\lambda = 4096/10$ takes far longer to move into the power-law regime where the JMAK predictions are feasible, over $\tau = 100$ iterations.

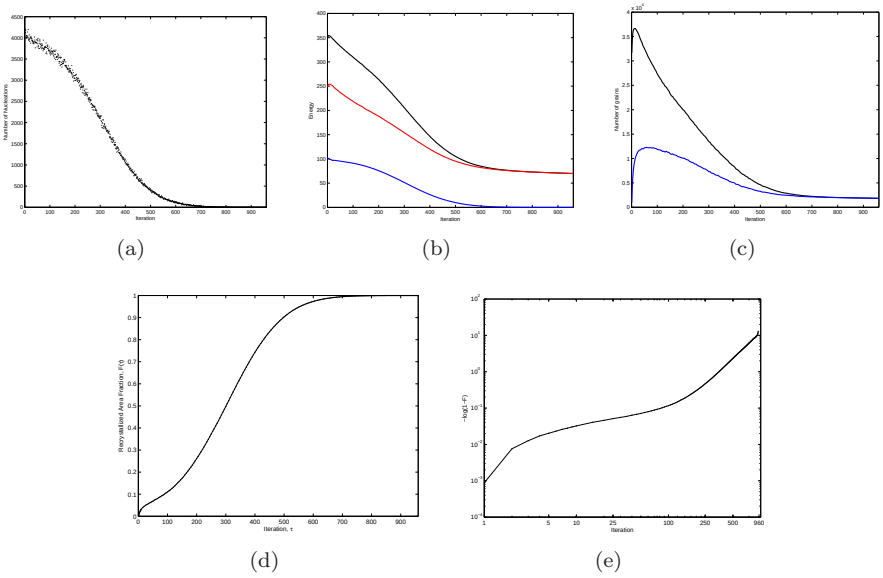

Figure 18: Statistics for the two-dimensional continuous rate nucleation with $\lambda = 4096/40$. (a) The number of grain nucleations is initially ≈ 4000 per time step, and decays as the recrystallized area fraction increases. A total of 1,246,777 grain nucleations occur during the simulation, though at no time are there more than 13,000 recrystallized grains present in the system. (b) The total energy (black) is the sum of bulk energy (blue) and interfacial energy (red). The interfacial energy increases initially and increases due to grain nucleations (which tend to increase the total interface length) but also decreases at each time step due to the curvature motion. Nucleations decrease the bulk energy. (c) The total number of grains is shown in black and the number of recrystallized grains is shown in blue. (d) The recrystallized area fraction F as a function of the number of iterations is presented. (e) A plot of $\log(1 - F(\tau))$ vs. (τ) is shown demonstrating that JMAK theory is not applicable in this example.

normally distributed with mean $4.9\Delta x$ and standard deviation $2.0\Delta x$. Each grid point corresponding to an unrecrystallized grain is selected to be the center of a nucleated grain with probability 2.5×10^{-4} at each time step.

Initially, when the recrystallized area fraction is very small, approximately $4,200$ nucleations are expected to occur in each time step. Figure 18(a) plots the number of nucleations in each time step. A total of $1,246,777$ nucleations occur in the entire simulation. Never are more than $13,000$ recrystallized grains present in the system at one time, and only $1,841$ recrystallized grains are present when the recrystallization concludes (Figure 18(c)).

Figure 18(b) shows the energy of the system as the evolution takes place. Because nucleation locations are chosen without regard to their effect on the system energy, the energy for this simulation increases in the first three time steps. Thereafter, the energy decreases constantly, since in addition to the evolution of unrecrystallized grains, many grain nuclei disappear in each iteration (helping to counterbalance the addition of new grain nuclei). This is demonstrated by Figure 18(c), showing the large increase in total number of grains initially, and the longer-lasting increase in number of recrystallized grains. Both these measures decrease as the evolution continues. Figure 18(d) shows the recrystallized area fraction F as a function of iterations performed (τ). Note that in these conditions, the function $F(\tau)$ does not appear to be sigmoidal initially. The deviation from JMAK theory is verified in Figure 18(e), where the relationship between iterations (τ) and $\log(1 - F(\tau))$ is shown to be poorly described by a power-law relationship in the early stages of the evolution.

The recrystallizing grain microstructure is shown in Figure 19. Unlike the site-saturated nucleation examples, the size of recrystallized grains varies significantly. At intermediate times, this is partially due to the presence of small, recently nucleated grains that will quickly disappear. Even at the final time, when recrystallization is complete, there is significant variation in the size of recrystallized grains due to their different lifespans, depending on when they nucleated.

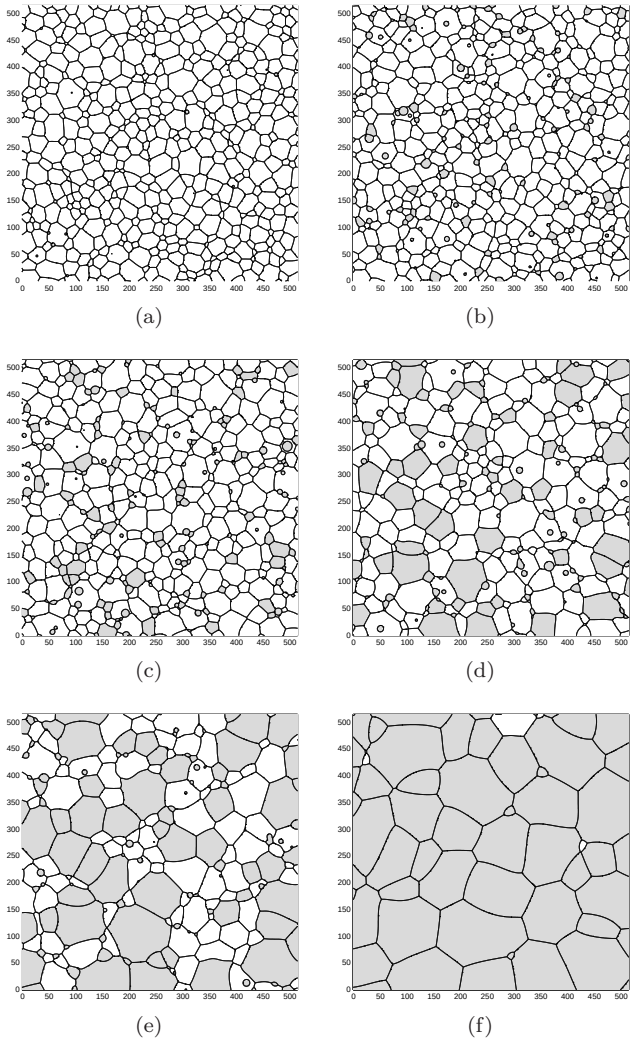

Figure 19: A 512×512 section of the two-dimensional recrystallizing grain pattern with $\lambda = 4096/40$ and continuous rate nucleation after (a) 1, (b) 25, (c) 75, (d) 195, (e) 300, and (f) 555 iterations. These correspond to 0.01%, 5.0%, 8.8%, 25.1%, 49.7%, and 95.0% recrystallized area, respectively. Recrystallized grains are shaded in gray. There are many nucleated grains completely contained within unrecrystallized grains at later times due to the continuous nucleation; however, these grains are very unlikely to survive.

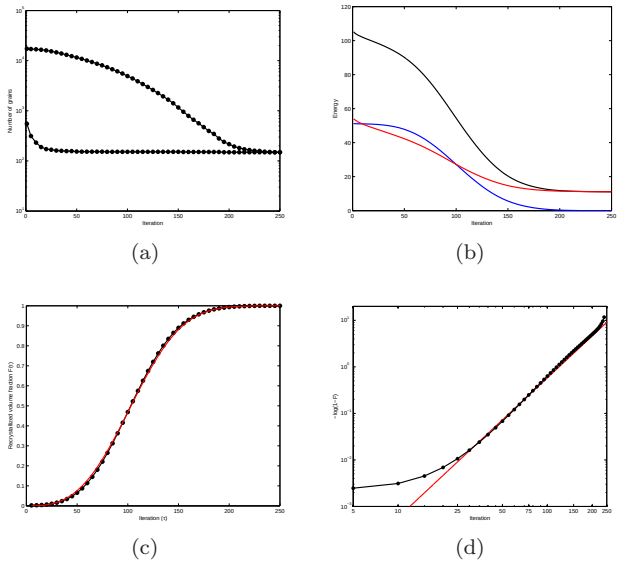

Figure 20: Three-dimensional site-saturated homogenous nucleation: (a) Logarithmic plot of the total number of grains (top) and number of recrystallized grains (bottom). Initially, recrystallized grains are on average much smaller that unrecrystallized grains. Only a few (approximately 150) survive and grow but these quickly come to dominate the unrecrystallized grains. (b) Evolution of the energy. Note that both the bulk energy (blue) and the interfacial energy red) decrease at each time step. The black line is the total energy, the sum of the interfacial and bulk energy terms. (c) Comparison of the recrystallized volume fraction computed from simulation (dotted) and fit to JMAK prediction $F(\tau) = 1-\exp(-k\tau^3)$, $k = 6.3\times10^{-7}$ (solid). (d) JMAK theory predicts a power-law relationship between $\log(1 - F(\tau))$ and iteration τ. For site-saturated homogeneous nucleation in three dimensions, the Avrami exponent is predicted to be 3 (appearing as a line with slope 3 (red) in the logarithmic plot of simulation data (dotted)).

4.7 Three-dimensional recrystallization

We perform two simulations of recrystallization in three dimensions on a $256 \times 256 \times 256$ discretization of $[0, 1]^3$. The same initial condition of unrecrystallized grains was used for both simulations. This initial condition contained 16,767 grains. As before, in both of our simulations all nucleation is equally likely to occur anywhere in the computational domain, without regard to the pre-existing microstructure.

In the first simulation, we perform site-saturated nucleation (all nucleation occurs at the initial time) in the heterogeneous nucleation regime of the parameter λ. We nucleate 960 spherical grains, with radii uniformly distributed in the range $[\Delta x, 6\Delta x]$ (where $\Delta x = 1/256$), and choose $\lambda = 256/10$. From (18), it is immediately clear that any spherical nucleated grain not intersecting a grain boundary (i.e., entirely contained in the interior of a single unrecrystallized grain) with radius less than $20\Delta x$ should shrink and disappear. Indeed, many of the nucleated grains disappear very quickly. Figure 20(a) shows the evolution of the total number of grains and the number of recrystallized grains. Only 552 recrystallized grains survive the first time step, as many of the small nucleated grains disappear immediately. See Figure 21 for snapshots of a slice of the three-dimensional evolution. As no new grains are nucleated in the system after initialization, the energy of the system decreases monotonically (Figure 20(b)).

For site-saturated nucleation in three dimensions, the value of p in (19) is predicted to be 3 [9]. In Figure 20(c), we plot the simulated recrystallized volume fraction against the fit $F(\tau) = 1 - \exp(-6.3 \times 10^{-7}\tau^3)$, where τ is the number of iterations ($\tau = t/\Delta t$), a simple linear rescaling of time. Figure 20(d) demonstrates the match of the simulation data to (19), with $p = 3$ (represented as a linear function with slope three on logarithmic axes). The simulation data does not fit the prediction well during a transition period early in the simulation ($\tau < 25$) but matches very well thereafter. This behavior (an initial transition period followed by good agreement with JMAK predictions) matches what is seen in two-dimensions for the equivalent parameter choice of $\lambda = n/10$, on a uniform grid of n grid points in each dimension.

The second simulation models continuous nucleation: at each time step, each unrecrystallized grid site has a fixed probability of nucleating a grain. We set the probability for a given unrecrystallized site to

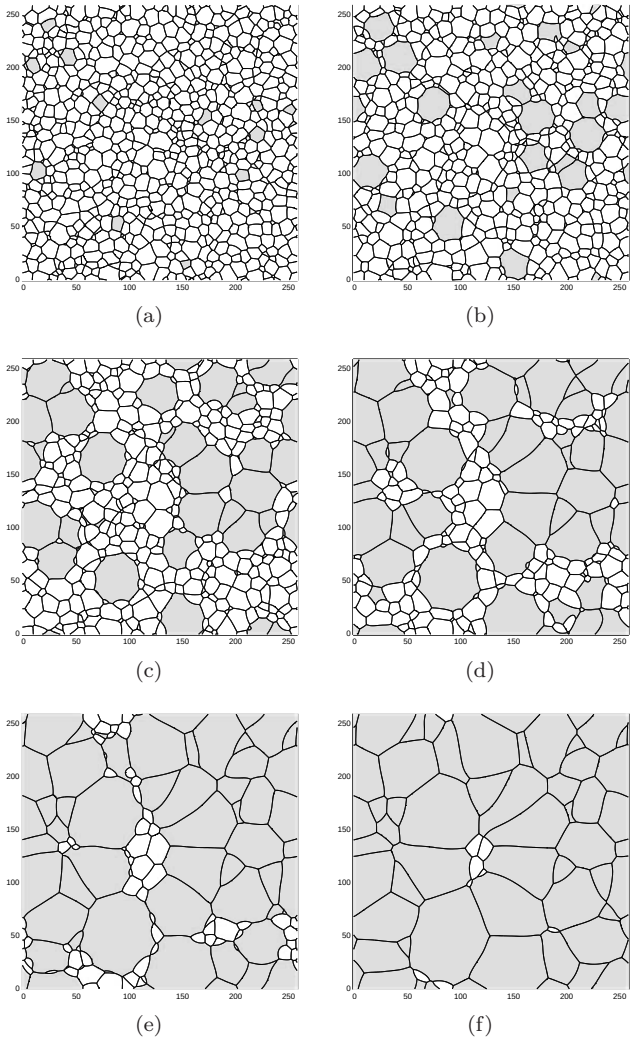

Figure 21: A slice of the three-dimensional recrystallizing grain pattern with site-saturated nucleation at (a) 1.1%, (b) 8.8%, (c) 26.5%, (d) 52.2%, (e) 76.2% and (f) 94.5% recrystallization. Recrystallized grains are shaded in gray.

nucleate a grain at each iteration to be 10^{-6}. This choice of probability predicts that $\approx$ 15–20 nucleations should occur in each time step when there are few recrystallized grain sites. Again we nucleate spherical grains, with radii uniformly distribution in $[\Delta x, 6\Delta x]$ and fix $\lambda = 256/10$, corresponding to $H/J = 0.2$, which was observed in two dimensions to fall into the heterogeneous nucleation regime. The evolution in the number of grains (both total and recrystallized) is shown in Figure 22(a). The number of recrystallized grains increases fastest early in the simulation, when there are many sites available for nucleation. Later in the simulation, the number of recrystallized grains decreases as there are few sites available for recrystallization and the curvature motion between recrystallized grains in contact with each other is the main force driving the evolution.

The energy of the system (subdivided into bulk energy and interfacial energy terms) is shown in Figure 22(b). In contrast to the energy for site-saturated nucleation (Figure 20(b)), this energy increases rapidly initially. The nucleation of new recrystallized grains is a discontinuous process and is performed randomly without regard to the change in energy of the system due to the nucleation. Small nucleated grains have a large surface area to volume ratio, and so tend to increase the interfacial energy of the system more than they decrease the bulk energy by replacing parts of unrecrystallized grains. This effect is especially noticeable in the first few time steps and is later covered by the more rapid growth of the larger nucleated grains.

For continuous nucleation, the recrystallized volume fraction, F, is predicted to satisfy (19) with $p = 4$ [9]. We find that the data fits to $F(\tau)$ well, with $k = 8.7 \times 10^{-9}$. Figure 22(d) shows the fit to the predicted Avrami exponent, comparing the simulation data and fitted functions via the transformation $-\log(1-F(\tau))$. Recall that for the choice $\lambda = 256/10$, the evolution is in the regime of heterogeneous nucleation and so is not expected to fit JMAK predictions tightly during the transition period at the start of the evolution.

Figure 23 shows the evolution of the recrystallization with continuous nucleation. The contrast between site-saturated (Figure 21) and continuous recrystallization is particularly noticeable at $\tau = 50, 100, 150$. Under continuous recrystallization, the recrystallized grains show greater variation in size than under site-saturated recrystallization. The difference is particularly well shown in the histograms of Figures 24 and 25. The distribution of grain radii is quite bimodal under site-saturation after the nucleated grains begin to grow large with respect to mean grain size, with clear separation between the distributions for unrecrystallized and recrystallized grains. In contrast, the distribution of recrystallized grain sizes is much wider under continuous nucleation. This is to be expected, as the recrystallized grains had different lifespans from which to grow from the initial nucleation sizes.

The process of nucleation is complex and not completely understood (see, for instance, [11]). However, the immediate disappearance of the majority of the nucleated grains mitigates the effect of the arbitrary choice made for the distribution of nucleated grain radii; and it is seen in Figures 21 and 23 that the recrystallized grains rapidly lose their initial spherical shape due to curvature-based interactions with the grain boundaries of the surrounding unrecrystallized grains. In the presence of a large λ value (as in some of our two-dimensional simulations), the bulk energy driving force would more heavily outweigh the curvature term and in this regime the initial condition used for grain nucleation would have much more impact on the final microstructure of recrystallized grains.

5 Summary and Conclusions

We apply the algorithm developed in [13,14] based on diffusion generated motion of signed distance functions to a three-dimensional simulation of grain growth. This approach naturally captures the Herring condition at triple junctions. In addition, numerical evidence unequivocally shows that the energy of the simulated system decays, even through topological changes. The efficiency of this algorithm allows us to compute the *accurate* evolution of over 130,000 grains until less than 15,000 grains remain. To the best of our knowledge, this evolution contained at least twice as many grains as any other currently published to date. In the next largest simulation, [53], the authors implement a phase field model initially containing 50,000 grains on a $512 \times 512 \times 512$ grid. Grains have an average initial size of approximately $14 \times 14 \times 14$ grid points, with a diffuse interface width ϵ of 3 grid points. This suggests that the initial resolution of their system is quite low. We are able to verify, with greater confidence, that the coarsening rate for normal grain growth is $\langle r \rangle \sim t^{1/2}$ and that the grain size distribution function is self-similar. We are also able to provide accurate average values of the number of edges, corners and faces of individual grains. We observe that in many cases these

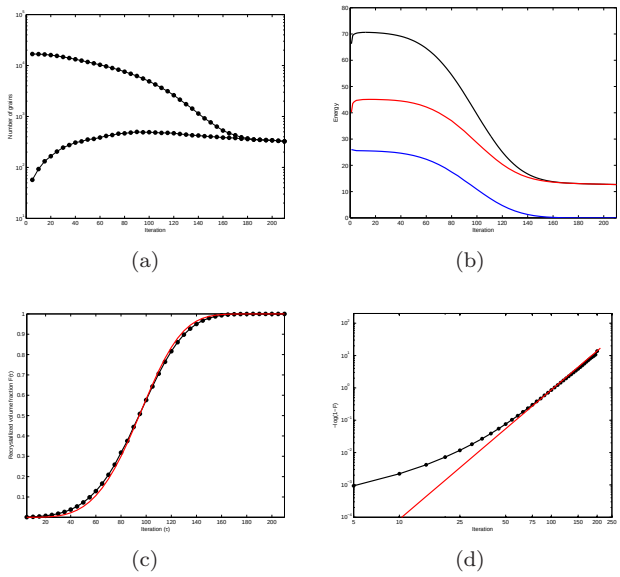

Figure 22: Three-dimensional continuous homogenous nucleation: (a) The total number of grains (top) and number of recrystallized grains (bottom). The number of recrystallized grains increases initially then decreases as the curvature motion becomes the dominant force in the evolution. (b) The total energy of the system (black), the bulk energy (blue), and the interfacial energy (red). The nucleation process is not part of the steepest descent evolution and does not guarantee a decrease in the system energy. (c) Fit of the recrystallized volume fraction $F(\tau)$ to $(1 - \exp(-8.7 \times 10^{-9}\tau^4))$ (red). (d) For continuous homogenous nucleation, the Avrami exponent is predicted to be 4 (represented as a linear function with slope 4 (red) on logarithmic axes).

are in agreement with experimental results. This provides further validation that normal grain growth is present in experimental settings.

We have extended the algorithm to include a model for recrystallization in both two and three dimensions. In this model the recrystallized grains have a bulk energy λ less than the unrecrystallized material, meaning that system's energy will be lowered if recrystallized grains grow into the unrecrystallized material. Good agreement with Johnson, Mehl, Avrami, and Kolmogorov (JMAK) theory is found here in the appropriate large-λ limit. In addition, our algorithm works well for λ that are physically reasonable (moderate λ). This is notable because Monte Carlo methods are reported not to work well in this regime. The evolution of the grains at moderate λ values is quite different from large λ because the critical size for nucleated grains is larger, and the pattern of nucleated grains becomes heterogeneous. Finally, we mention that although these results are not presented here, we have numerically verified that as $\lambda \to \infty$, the vanishing surface tension limit of Reitich and Soner [40] is also obtained by the algorithms presented.

Acknowledgements

This work was supported, in part, by grants from the National Science Foundation: DMS-0748333 and DMS-0810113. Selim Esedoglu was also supported by an Alfred P. Sloan Foundation fellowship.

References

[1] Aboav, D. A. The arrangement of grains in a polycrystal. *Metall. 3* (1970), 383–390.

[2] Anderson, M. P., Grest, G. S., and Srolovitz, D. J. Computer simulation of normal grain growth in three dimensions. *Philos. Mag. B 59*, 3 (1989), 293–329.

[3] Avrami, M. Kinetics of phase change. I. General theory. *J. Chem. Phys. 7* (1939), 1103–1112.

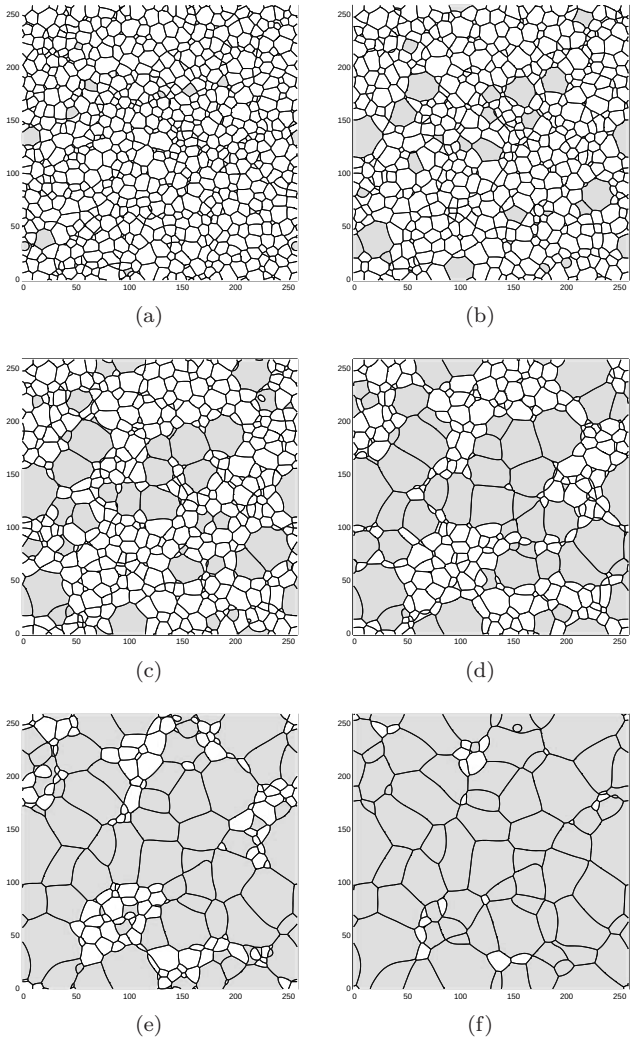

Figure 23: A slice of the three-dimensional recrystallizing grain pattern with continuous nucleation at (a) 1.2%, (b) 9.8%, (c) 25.9%, (d) 50.9%, (e) 76.4%, and (f) 95.0% recrystallization. Recrystallized grains are shaded in gray.

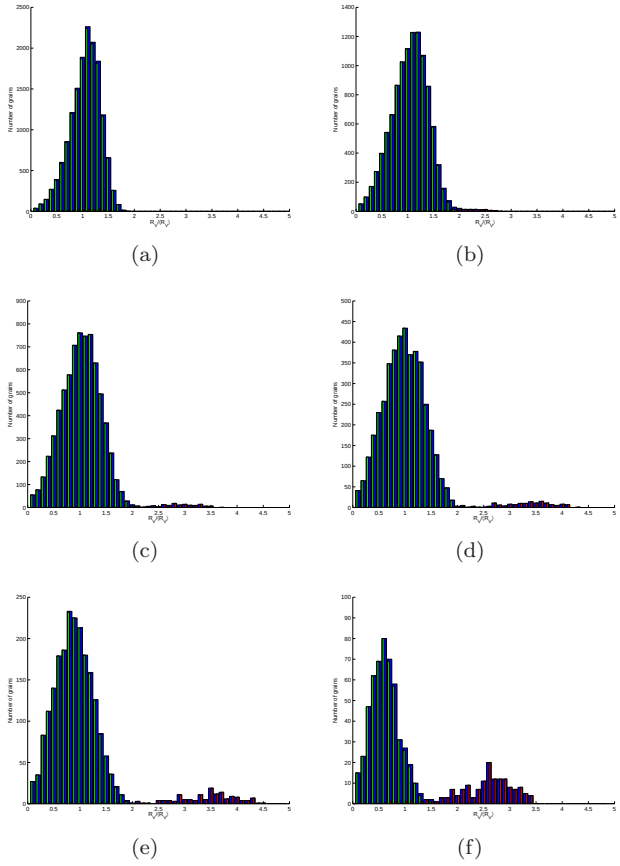

Figure 24: Histogram of relative grain sizes for three-dimensional site-saturated nucleation at (a) 1.1%, (b) 8.8%, (c) 26.5%, (d) 52.2%, (e) 76.2% and (f) 94.5% recrystallization. All grains are represented in blue bars. Each blue bar is subdivided into green and red sub-bars, representing the number of unrecrystallized and recrystallized grains, respectively. Initially the recrystallized grains are much smaller than the unrecrystallized grains, but that at later times, the recrystallized grains are much larger, on average. Recall from Figure 20(a) that the total number of recrystallized grains changes very little after the first 25 iterations.

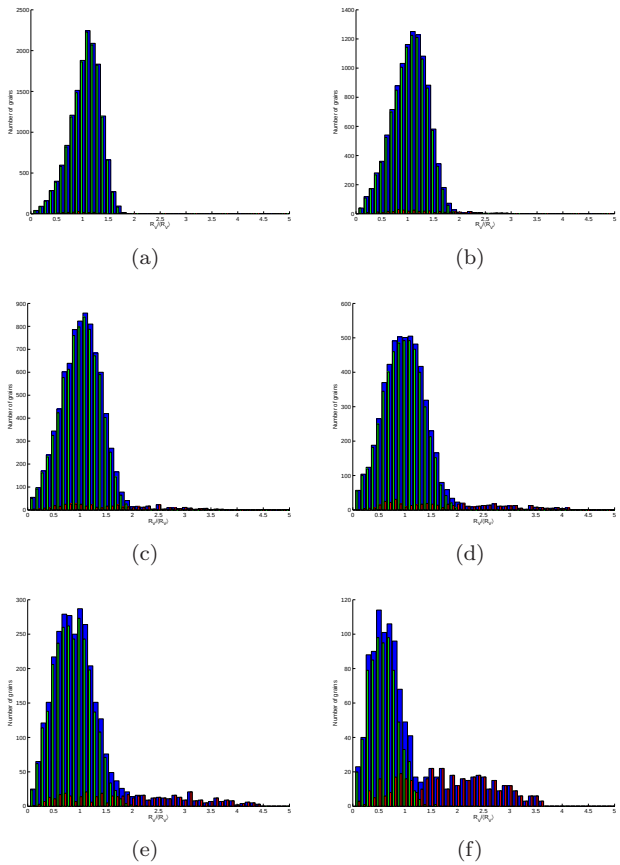

Figure 25: Histogram of relative grain sizes for three-dimensional continuous nucleation at (a) 1.2%, (b) 9.8%, (c) 25.9%, (d) 50.9%, (e) 76.4%, and (f) 95.0% recrystallization. All grains are represented in blue bars. Each blue bar is subdivided into green and red sub-bars, representing the number of unrecrystallized and recrystallized grains, respectively. Small recrystallized grains are present in higher frequencies than under site-saturated nucleation (compare to Figure 24).

[4] Avrami, M. Kinetics of phase change. II. Transformation-time relations for random distribution of nuclei. *J. Chem. Phys. 8* (1940), 212–224.

[5] Avrami, M. Kinetics of phase change. III. Granulation, phase change, and microstructure. *J. Chem. Phys. 9*, 2 (1941), 177–184.

[6] Beck, P. Interface migration in recrystallization. In *Metal Interfaces*, R. Brick, Ed. American Society for Metals, Cleveland, 1952, pp. 208–247.

[7] Bernacki, M., Resk, H., Coupez, T., and Logé, R. E. Finite element model of primary recrystallization in polycrystalline aggregates using a level set framework. *Model. Simul. Mater. Sci. Eng. 17* (2009), 064006.

[8] Burke, J. E., and Turnbull, D. Recrystallization and grain growth. *Prog. Met. Phys. 3* (1952), 220–292.

[9] Christian, J. W. *Theory of transformations in metals and alloys*, 2 ed. Pergamon, Oxford, 1975. Page 542.

[10] Desch, C. H. The solidification of metals from the liquid state. *J. Inst. Metals 22*, 2 (1919), 241–276.

[11] Doherty, R. D., Hughes, D. A., Humphreys, F. J., Jonas, J. J., Jensen, D. J., Kassner, M. E., King, W. E., McNelley, T. R., McQueen, H. J., and Rollett, A. D. Current issues in recrystallization: a review. *Mater. Sci. Eng. A238* (1997), 219–274.

[12] Edwards, S. F., and Pithia, K. D. A note on the Aboav–Weaire law. *Phys. A 205* (1994), 577–584.

[13] Elsey, M., Esedoḡlu, S., and Smereka, P. Diffusion generated motion for grain growth in two and three dimensions. *J. Comp. Phys 228* (2009), 8015–8033.

[14] Esedoḡlu, S., Ruuth, S., and Tsai, R. Diffusion generated motion using the distance function. Tech. rep., UCLA, 2009. CAM Report 09–29, to appear in *J. Comp. Phys.*

[15] Esedoḡlu, S., and Smereka, P. A variational formulation for a level set representation of multiphase flow and area preserving curvature flow. *Commun. Math. Sci. 6*, 1 (2008), 125–148.

[16] Fan, D., and Chen, L.-Q. Computer simulation of grain growth using a continuum field model. *Acta Mater. 45*, 2 (1997), 611–622.

[17] Fayad, W., Thompson, C. V., and Frost, H. J. Steady-state grain-size distributions resulting from grain growth in two dimensions. *Scr. Mater. 40*, 10 (1999), 1199–1204.

[18] Feltham, P. Grain growth in metals. *Acta Metall. 5* (1957), 97–105.

[19] Garcke, H., Nestler, B., and Stoth, B. A multiphase field concept: Numerical simulations of moving phase boundaries and multiple junctions. *SIAM J. Appl. Math. 60*, 1 (1999), 295–315.

[20] Harker, D., and Parker, E. Grain shape and grain growth. *Trans. Am. Soc. Met. 34* (1945), 156–201.

[21] Herring, C. Surface tension as a motivation for sintering. In *The Physics of Powder Metallurgy*, W. Kingston, Ed. McGraw–Hill, New York, 1951, pp. 143–179.

[22] Hesselbarth, H. W., and Göbel, I. R. Simulation of recrystallization by cellular automata. *Acta Metall. Mater. 39*, 9 (1991), 2135–2143.

[23] Hillert, M. On the theory of normal and abnormal grain growth. *Acta Metall. 13* (1965), 227–238.

[24] Hull, F. C. Plane section and spatial characteristics of equiaxed β-brass grains. *Mater. Sci. Technol. 4* (1988), 778–785.

[25] Johnson, W. A., and Mehl, R. F. Reaction kinetics in processes of nucleation and growth. *Trans. Am. Inst. Min. Metall. Eng. 135* (1939), 416–442.

[26] Kawasaki, K., Nagai, T., and Nakashime, K. Vertex models for two-dimensional grain growth. *Philos. Mag. B 60*, 3 (1989), 399–421.

[27] Kim, S. G., Kim, D. I., Kim, W. T., and Park, Y. B. Computer simulations of two-dimensional and three-dimensional ideal grain growth. *Phys. Rev. E 74* (2006), 061605.

[28] Kinderlehrer, D., Lee, J., Livshits, I., Rollett, A., and Ta'asan, S. Mesoscale simulation of grain growth. *Mater. Sci. Forum 67–70* (2004), 1057–1062.

[29] Kolmogorov, A. N. On the statistical theory of crystallization in metals. *Bull. Acad. Sci. USSR. Ser. Math. 3* (1937), 367–368.

[30] Krill III, C. E., and Chen, L.-Q. Computer simulation of 3-D grain growth using a phase-field model. *Acta Mater. 50* (2002), 3057–3073.

[31] Liu, G., Yu, H., Song, X., and Qin, X. A new model of three-dimensional grain growth: theory and computer simulation of topology-dependency of individual grain growth rate. *Mater. Des. 22* (2001), 33–38.

[32] Louat, N. P. On the theory of normal grain growth. *Acta Metall. 22* (1974), 721–724.

[33] MacPherson, R., and Srolovitz, D. The von Neumann relation generalized to coarsening of three-dimensional microstructures. *Nature 446* (2007), 1053–1055.

[34] Mantegazza, C., Novaga, M., and Tortorelli, V. M. Motion by curvature of planar networks. *Ann. Scuola Norm. Super. Pisa–Cl. Sci. 3*, 2 (2004), 235–324.

[35] Meijering, J. L. Interface area, edge length, and number of vertices in crystal aggregates with random nucleation. *Phillips Res. Rep. 8* (1953), 270–290.

[36] Merriman, B., Bence, J. K., and Osher, S. Motion of multiple junctions: a level set approach. *J. Comput. Phys. 112*, 2 (1994), 334–363.

[37] Mullins, W. W. Two-dimensional motion of idealized grain boundaries. *J. Appl. Phys. 27*, 6 (1956), 900–904.

[38] Mullins, W. W. Estimation of the geometrical rate constant in idealized three dimensional grain growth. *Acta Metall. 37*, 11 (1989), 2979–2984.

[39] Piękoś, K., Tarasiuk, J., Wierzbanowski, K., and Bacroix, B. Generalized vertex model of recrystallization — application to polycrystalline copper. *Comuptational Materials Science 42* (2008), 584–594.

[40] Reitich, F., and Soner, H. M. Three-phase boundary motion under constant velocities. I: The vanishing surface tension limit. *Proc. R. Soc. Edin. 126A* (1996), 837–865.

[41] Rhines, F. R., and Patterson, B. R. Effect of the degree of prior cold work on the grain volume distribution and the rate of grain growth of recrystallized aluminum. *Metall. Trans. A 13* (1982), 985–993.

[42] Rios, P. R., Dalpian, T. G., Brandão, V. S., Castro, J. A., and Oliveira, A. C. L. Comparison of analytical grain size distributions with three-dimensional computer simulations and experimental data. *Scr. Mater. 54* (2006), 1633–1637.

[43] Rollett, A. D., and Raabe, D. A hybrid model for mesoscopic simulation of recrystallization. *Comput. Mater. Sci. 21* (2001), 69–78.

[44] Russo, G., and Smereka, P. A remark on computing distance functions. *J. Comput. Phys. 163* (2000), 51–67.

[45] Ruuth, S. J. A diffusion-generated approach to multiphase motion. *J. Comput. Phys. 145* (1998), 166–192.

[46] Ruuth, S. J. Efficient algorithms for diffusion-generated motion by mean curvature. *J. Comput. Phys. 144* (1998), 603–625.

[47] Smereka, P. The numerical approximation of a delta function with application to level set methods. *J. Comput. Phys 211*, 1 (2006), 77–90.

[48] Smith, C. S. Grain shapes and other metallurgical applications of topology. In *Metal Interfaces*, R. Brick, Ed. American Society for Metals, Cleveland, 1952, pp. 65–114.

[49] Smith, C. S. Some elementary principles of polycrystalline microstructure. *Met. Rev. 9*, 33 (1964), 1–48.

[50] Srolovitz, D. J., Grest, G. S., and Anderson, M. P. Computer simulation of grain growth — V. Abnormal grain growth. *Acta Metall. 33*, 12 (1985), 2233–2247.

[51] Srolovitz, D. J., Grest, G. S., and Anderson, M. P. Computer simulation of recrystallization — I. Homogeneous nucleation and growth. *Acta Metall. 34*, 9 (1986), 1833–1845.

[52] Srolovitz, D. J., Grest, G. S., Anderson, M. P., and Rollett, A. D. Computer simulation of recrystallization — II. Heterogeneous nucleation and growth. *Acta Metall. 36*, 8 (1988), 2115–2128.

[53] Suwa, Y., Saito, Y., and Onodera, H. Parallel computer simulation of three-dimensional grain growth using the multi-phase-field model. *Mater. Trans. 49*, 4 (2008), 704–709.

[54] Wakai, F., Enomoto, N., and Ogawa, H. Three-dimensional microstructural evolution in ideal grain growth — general statistics. *Acta Mater. 48* (2000), 1297–1311.

[55] Wakai, F., Shinoda, Y., Ishihara, S., and Dominguez-Rodriguez, A. Topological transformation of grains in three-dimensional normal grain growth. *J. Mater. Res. 16* (2001), 2136–2142.

[56] Weaire, D. Some remarks on the arrangement of grains in a polycrystal. *Metall. 7* (1974), 157–160.

[57] Weaire, D., and Glazier, J. A. Relation between volume, number of faces and three-dimensional growth laws in coarsening cellular patterns. *Philos. Mag. Lett. 68*, 6 (1993), 363–365.

[58] Weygand, D., and Bréchet. Three-dimensional grain growth: a vertex dynamics simulation. *Philos. Mag. B 79*, 5 (1999), 703–716.

[59] Williams, R. E. Space-filling polyhedron: Its relation to aggregates of soap bubbles, plant cells, and metal crystallites. *Science 161*, 3838 (1968), 276–277.

[60] Williams, W. M., and Smith, C. S. A study of grain shape in an aluminum alloy and other applications of stereoscopic microradiography. *Trans. Am. Inst. Min. Met. Eng. 194* (1952), 755–765.

[61] Zhang, C., Suzuki, A., Ishimaru, T., and Enomoto, M. Characterization of three-dimensional grain structure in polycrystalline iron by serial sectioning. *Metall. Mater. Trans. A 35A* (2004), 1927–1933.

[62] Zhao, H.-K. A fast sweeping method for Eikonal equations. *Math. Comput. 74*, 250 (2004), 603–627.

[63] Zhao, H.-K., Chan, T., Merriman, B., and Osher, S. A variational level set approach to multiphase motion. *J. Comput. Phys. 127* (1996), 179–195.